





















A High-resolution Study of the Cold Neutral Medium in and around 30 Doradus

GYUEUN PARK ^{1,2} MIN-YOUNG LEE ^{1,2} JOHN M. DICKEY ³ NICK M. PINGEL ⁴ JAMES DEMPSEY ⁵ HELGA DÉNES ^{6,7}
STEVEN GIBSON ⁸ KATIE JAMESON ⁹ IAN KEMP ^{10,11} CHANG-GOO KIM ¹² DENIS LEAHY ¹³ BUMHYUN LEE ¹⁴ CALLUM LYNN ⁵
YIK KI MA ^{5,15} ANTOINE MARCHAL ⁵ NAOMI M. McCLURE-GRIFFITHS ⁵ ERIC MULLER ⁵ HIEP NGUYEN ⁵ SNEŽANA STANIMIROVIĆ ⁴
AND JACCO TH. VAN LOON ¹⁶

THE GASKAP-H I COLLABORATION

¹Korea Astronomy & Space Science Institute, 776 Daedeok-daero, Yuseong-gu, Daejeon 34055, Republic of Korea

²Department of Astronomy and Space Science, University of Science and Technology, 217 Gajeong-ro, Yuseong-gu, Daejeon 34113, Republic of Korea

³School of Natural Sciences, Private Bag 37, University of Tasmania, Hobart, TAS, 7001, Australia

⁴Department of Astronomy, University of Wisconsin-Madison, 475 N. Charter St., Madison, WI 53703, USA

⁵Research School of Astronomy and Astrophysics, The Australian National University, Canberra, ACT 2611, Australia

⁶School of Physical Sciences and Nanotechnology, Yachay Tech University, Hacienda San José S/N, 100119, Urcuquí, Ecuador

⁷College of Sciences and Engineering, Universidad San Francisco de Quito, Quito, Ecuador

⁸Department of Physics and Astronomy, Western Kentucky University, Bowling Green, KY 42101, USA

⁹Caltech Owens Valley Radio Observatory, Pasadena, CA 91125, USA

¹⁰International Centre for Radio Astronomy Research (ICRAR), Curtin University, Bentley, WA 6102, Australia

¹¹CSIRO Space and Astronomy, 26 Dick Perry Avenue, Kensington, 6151, WA, Australia

¹²Department of Astrophysical Sciences, Princeton University, 4 Ivy Lane, Princeton, NJ 08544, USA

¹³Department of Physics & Astronomy, University of Calgary, Calgary, AB T2N 1N4, Canada

¹⁴Department of Astronomy, Yonsei University, 50 Yonsei-ro, Seodaemun-gu, Seoul 03722, Republic of Korea

¹⁵Max-Planck-Institut für Radioastronomie, Auf dem Hügel 69, 53121 Bonn, Germany

¹⁶Lennard-Jones Laboratories, Keele University, ST5 5BG, UK

(Accepted December 3, 2025)

ABSTRACT

With the aim of evaluating the roles of the cold neutral medium (CNM) in the cloud-scale baryon cycle, we perform a high-resolution study of the CNM in and around the extreme star-forming region 30 Doradus (30 Dor). For our study, we use Galactic Australian Square Kilometre Array Pathfinder H I Survey data and produce H I emission and absorption cubes on 7 pc scales. To examine the CNM structures toward 30 Dor, we decompose the H I absorption cube into 862 Gaussian components and find that these components are distributed at four velocity ranges (B1, B2, B3, and B4, respectively): 200–230 km s^{−1}, 230–260 km s^{−1}, 260–277 km s^{−1}, and 277–300 km s^{−1}. We derive line-of-sight average spin temperatures and opacity-corrected total H I column densities and show that the B1–B4 structures have systematically different properties, indicating that they are physically distinct. As for the nature of the observed CNM structures, we find that B2 is associated with the main dense structure where ionized, atomic, and molecular gases are concentrated. B3 and B4 trace inflows whose combined mass flux rate of 0.14 M_⊙ yr^{−1} is comparable to the current star formation rate, while B1 probes outflows with a much lower mass flux rate of 0.007 M_⊙ yr^{−1}. Interestingly, the H I column densities in B1–B4 are nearly uniform with a factor of two spatial variations, implying the presence of H I shielding layers for H₂ formation.

Keywords: Cold neutral medium (266) — H II regions (694) — Interstellar absorption (831) — Interstellar atomic gas (833) — Interstellar phases (850) — Interstellar molecules (849) — Interstellar medium

(847) — Large Magellanic Cloud (903) — Molecular clouds (1072) — Photodissociation regions (1223) — Radio astronomy (1338)

1. INTRODUCTION

Molecular clouds (MCs) are the coldest and densest component of the interstellar medium (ISM) and the primary stellar nurseries (e.g., R. C. Kennicutt & N. J. Evans 2012). Recent theoretical and observational studies have demonstrated that a range of processes on the scales of individual MCs control the evolution of galaxies (e.g., M. R. Krumholz & C. F. McKee 2005; J. M. D. Kruijssen & S. N. Longmore 2014; M. Chevance et al. 2020; J. Kim et al. 2022). These processes encompass the accretion of raw materials, the transition from atomic (H I) to molecular hydrogen (H₂), star formation, and the destruction of MCs via stellar feedback, forming the complex cloud-scale baryon cycle.

H I is a fundamental element in the cloud-scale baryon cycle and consists of the cold and warm neutral medium (CNM and WNM) with typical densities and kinetic temperatures of (n , T_k) \sim (7–70 cm⁻³, 60–260 K) and (0.2–0.9 cm⁻³, 5000–8300 K) for solar neighborhood conditions (e.g., C. F. McKee & J. P. Ostriker 1977; M. G. Wolfire et al. 2003; S. Bialy & A. Sternberg 2019). The segregation into the CNM and WNM is not very strict, as observations have shown that 20–30% of H I exist in an intermediate regime of the thermally unstable medium (UNM; e.g., C. Heiles & T. H. Troland 2003; C. E. Murray et al. 2018). Among the three phases of H I, the CNM is expected to play an important role in the H I-to-H₂ transition and star formation, thanks to its high density and low temperature. This expectation has been corroborated by recent observations that found molecular gas preferentially forms in environments with low spin temperatures $T_s \lesssim 100$ K and high CNM-to-total H I column density ratios $f(\text{CNM}) \sim 0.6$ (D. R. Rybarczyk et al. 2022; G. Park et al. 2023).

In spite of its importance in the cloud-scale baryon cycle, the CNM in and around individual MCs remains largely unexplored. This is because the CNM has been mainly studied via H I absorption measurements toward background continuum sources that are distributed over a large area of sky. To address the limitation of previous observations and shed light on the roles of the CNM in the cloud-scale baryon cycle, we focused on 30 Doradus (30 Dor hereafter) in the Large Magellanic Cloud (LMC), whose extensive continuum emission enabled us to spatially map H I absorption across the surface of the giant H II region.

Our target 30 Dor is the most extreme star-forming region in the Local Group of galaxies. It hosts more than 1000 OB-type and Wolf-Rayet stars (e.g., E. I. Doran et al. 2013) and produces ~ 500 times more ionizing photons than the Orion Nebula (e.g., E. W. Pellegrini et al. 2010). At the center of 30 Dor lies the super star cluster R136 with an exceedingly high

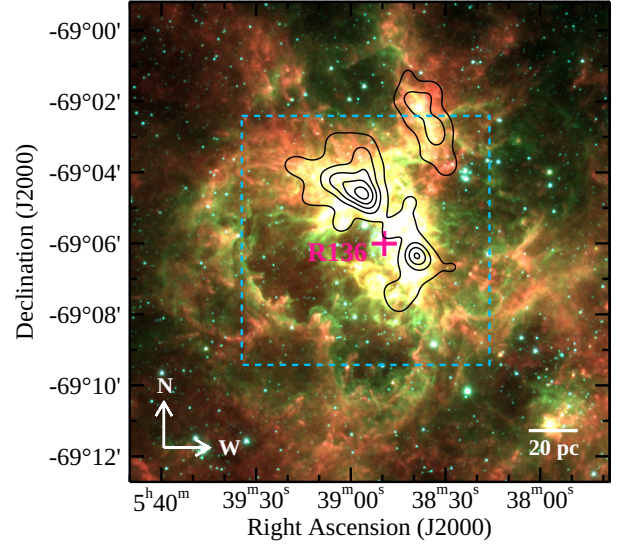


Figure 1. Three-color composite image of 30 Dor (*Spitzer* 8, 4.5, and 3.6 μm emission in red, green, and blue, respectively; M. Meixner et al. 2006). The CO integrated intensity image from T. Wong et al. (2022) is overlaid as the black contours with levels ranging from 10% to 90% of the maximum value of 44.1 K km s⁻¹ with increments of 20%. The blue box outlines the coverage of the GASKAP-H I data, while the red cross marks the location of the central star cluster R136.

stellar mass density of $\gtrsim 10^7 M_\odot \text{pc}^{-3}$ (F. J. Selman & J. Melnick 2013). This extraordinary star cluster harbors the most massive stars known ($\gtrsim 150 M_\odot$; P. A. Crowther et al. 2010) and constitutes almost half of the stellar mass in 30 Dor (E. I. Doran et al. 2013). Strong stellar winds and supernova explosions (SNe) created vast cavities and bubbles that fill 30 Dor with bright H α and X-ray emission (e.g., Y.-H. Chu & R. C. Kennicutt 1994; L. K. Townsley et al. 2006). Overall 30 Dor has been well examined at multi-wavelengths for star formation activities, as well as for gas and dust contents (e.g., L. K. Townsley et al. 2006; E. W. Pellegrini et al. 2010; E. I. Doran et al. 2013; R. Indebetouw et al. 2013; J. Roman-Duval et al. 2014; M. Y. Lee et al. 2019; T. Wong et al. 2022; O. Nayak et al. 2023), thanks to its proximity to the Milky Way (50 kpc; G. Pietrzyński et al. 2013) and unique half-solar metallicity condition (S. C. Russell & M. A. Dopita 1992). Our study fills a critical gap in the previous studies at 1.4 GHz, providing the first comprehensive view on the properties of the CNM in and around 30 Dor.

The Galactic Australian Square Kilometre Array Pathfinder H I Survey (GASKAP-H I; J. M. Dickey et al. 2013) is the key to the success of our study. This survey aims to reveal the structure, kinematics, and thermodynamics of H I in the Milky Way, Magellanic Clouds, and their sur-

roundings with an unprecedented combination of sensitivity and resolution using the Australian Square Kilometre Array Pathfinder (ASKAP) telescope. The most innovative aspect of the ASKAP telescope would be the phased array feed (PAF) that is mounted on the focal planes of 36 12m telescopes (A. W. Hotan et al. 2021). Up to 36 dual-polarization beams can be formed for each PAF-mounted telescope, resulting in a high survey speed with a wide field-of-view (FoV) of ~ 30 deg² at 1.4 GHz. The baselines range from 22 m to 6 km (630 in total), but most of them fall in two groups: one with lengths of 400–1200 m and the other with lengths of 2–3 km. The first peak of the baseline distribution gives an excellent brightness sensitivity for detecting weak H I emission at beam sizes of 30–60'', while the second peak enables us to obtain sensitive H I absorption spectra on 10'' scales. The capabilities of the GASKAP-H I survey were confirmed via Phase I and II pilot surveys (N. M. McClure-Griffiths et al. 2018; N. M. Pingel et al. 2022), and the full survey operation began in late 2024. Our study is based on the Phase II pilot observations of the LMC, whose coverage for 30 Dor is outlined in Figure 1.

This paper is organized as follows. In Section 2, we describe the GASKAP-H I observations and data reduction processes and present [C II] 158 μ m and ¹²CO(2–1) (CO hereafter) data. In Sections 3 and 4, we examine the structure of the CNM in and around 30 Dor based on Gaussian decomposition of H I absorption spectra and derive the physical properties of the CNM such as line-of-sight (LOS) average spin temperatures and opacity-corrected total H I column den-

ties. In addition, we probe the multi-phase structures of 30 Dor based on a comparison between the CNM, [C II], and CO spatial distributions and investigate how different the CNM in and around 30 Dor is compared to that in the Milky Way and the less star-forming part of the LMC. Finally, we discuss and summarize our results in Sections 5 and 6.

2. DATA

2.1. H I

2.1.1. GASKAP-H I Observations

The GASKAP-H I observations of the LMC were carried out as part of the Phase II pilot survey and were divided into five zones with Scheduling Blocks (SBs)¹⁷ of 33047, 38373, 38791, 38814, and 38845. Out of the total 108 observations for the SB33047 field (36 beams \times 3 interleaves), five measurement sets were chosen for imaging, whose specifications are listed in Table 1. We refer the readers to Section 2 of N. M. Pingel et al. (2022) for details on the GASKAP-H I observations.

The raw data were calibrated using ASKAPsoft (J. Guzman et al. 2019). This custom pipeline calibrates the band-pass, flags bad data, and performs self-calibration (amplitude and phase). We refer the readers to Section 11 of A. W. Hotan et al. (2021) and Section 3.1 of N. M. Pingel et al. (2022) for details on the calibration process. In the subsequent sections, we describe how we processed the calibrated data to produce H I absorption (“high-resolution”) and emission (“low-resolution”) cubes, as well as continuum maps.

Table 1. Specifications of the GASKAP-H I Observations (SB33047)

| Interleave | Beam | t_{on} | ν_0 | $\Delta\nu$ | BW | α_{J2000} | δ_{J2000} | Obs. Start | Obs. End |
|------------|------|-----------------|-----------|-------------|--------|-------------------------|-------------------------|-------------------|------------------|
| | | (hrs) | (MHz) | (kHz) | (kHz) | (hh:mm:ss) | (dd:mm:ss) | (UTC; hrs) | (UTC; hrs) |
| (1) | (2) | (3) | (4) | (5) | (6) | (7) | (8) | (9) | (10) |
| A | 21 | 3.54 | 1419.7228 | 1.157 | 2444.4 | 05:40:46.8 | −69:28:08 | 2021.10.27, 16.28 | 2021.10.28, 2.61 |
| A | 27 | 3.54 | 1419.7228 | 1.157 | 2444.4 | 05:35:42.3 | −68:41:29 | 2021.10.27, 16.28 | 2021.10.28, 2.61 |
| B | 20 | 3.57 | 1419.7228 | 1.157 | 2444.4 | 05:35:40.0 | −69:12:40 | 2021.10.27, 16.54 | 2021.10.28, 2.86 |
| C | 20 | 3.61 | 1419.7228 | 1.157 | 2444.4 | 05:35:37.7 | −69:43:50 | 2021.10.27, 16.79 | 2021.10.28, 3.12 |
| C | 27 | 3.61 | 1419.7228 | 1.157 | 2444.4 | 05:40:41.8 | −68:56:58 | 2021.10.27, 16.79 | 2021.10.28, 3.12 |

NOTE—(1) Interleave type; (2) Beam number; (3) On-source integration time; (4) Central frequency; (5) Spectral resolution (corresponding to a velocity resolution of 0.24 km s^{−1}); (6) Total bandwidth; (7, 8) Pointing center in the equatorial coordinate system (right ascension and declination in J2000); (9, 10) Observation date and time range.

¹⁷ The data and associated diagnostic reports are accessible from the CSIRO ASKAP Science Data Archive (CASDA; <https://data.csiro.au/collections/domain/casdaObservation/search/>).

2.1.2. High-Resolution Imaging

We employed the *tclean* task in Common Astronomy Software Application (CASA; CASA Team et al. 2022) to im-

Table 2. Imaging parameters

| Parameter | Resolution | |
|---------------------------------|----------------|-------------------|
| | High (13'') | Low (30'') |
| (1) imsize (pixels) | 3600 × 3600 | 1024 × 1024 |
| (2) cell (") | 1 | 7 |
| (3) reffreq (GHz) | 1.42040571183 | 1.42040561183 |
| (4) width (km s ⁻¹) | 0.977192 | 0.244212 |
| (5) restfreq (GHz) | 1.420405752000 | 1.420405752000 |
| (6) gridded | mosaic | IDG ^a |
| (7) deconvolver | multiscale | multiscale |
| (8) scales | 0, 12, 24, 36 | auto ^b |
| (9) weighting | Briggs | Briggs |
| (10) robust | 0.5 | 0 |
| (11) niter | 1E+08 | 1E+04 |
| (12) threshold (mJy) | 6.3 | 15 |
| (13) uvrange | all baselines | all baselines |

NOTE—(1) Image size; (2) Pixel size; (3) Reference frequency; (4) Channel width; (5) Rest frequency; (6) Gridding option; (7) Minor cycle algorithm; (8) Scale sizes for the multiscale algorithm; (9) Weighting scheme; (10) Robustness parameter for the Briggs weighting; (11) Maximum number of iterations; (12) Stopping threshold; (13) uv range for data selection.

^aImage Domain Gridded; S. van der Tol et al. (2018).

^bIn this mode, WSClean automatically sets the scales and uses as many as necessary. The first two scales include the delta scale (0) and the synthesized beam in terms of pixels. Subsequent scales are added by continually multiplying the synthesized beam scale by a factor of two until the scale size becomes larger than the image size.

age a $1^\circ \times 1^\circ$ cube centered on $(\alpha, \delta)_{J2000} = (05^h38^m36.6^s, -69^\circ05'56'')$. This cube is close to the size of the ASKAP primary beam at 1.4 GHz and has a velocity resolution of $\sim 1 \text{ km s}^{-1}$ (four times the native spectral resolution)¹⁸. For deconvolution, we used the multiscale CLEAN algorithm (T. J. Cornwell 2008). Specifically, we generated the cube with a pixel size of $1''$, scale sizes in increments of 12 from 0 to 36 ($0''$ – $36''$ for the diameter of the clean component; 0–2.8 times the synthesized beam), and a maximum iteration count of $1\text{E}+08$. In addition, we adopted a stopping threshold of 6.3 mJy based on three times the median standard deviation of the off-line channels (150 – 200 km s^{-1} and 320 – 380 km s^{-1}) in the dirty image. As the gridding option, we selected mosaic since our visibilities include many

¹⁸ In this paper, all velocities are quoted in the kinematic local standard of rest (LSRK) frame.

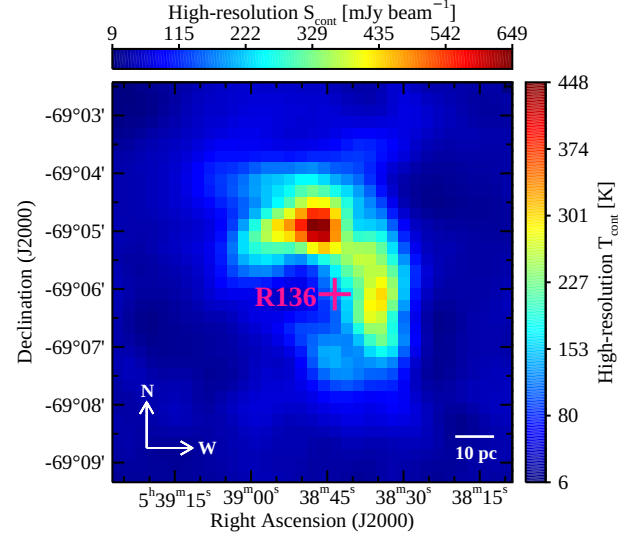


Figure 2. 1.4 GHz continuum image at a resolution of $30''$ with a pixel size of $12''$. The location of R136 is indicated as the red cross.

different pointing centers based on the PAFs (A. W. Hotan et al. 2021). Finally, we weighted the gridded data using the Briggs scheme with a robustness of 0.5 and produced the cube with a synthesized beam of $13.3'' \times 12.3''$. The adopted *tclean* parameters are summarized in Table 2.

To produce a high-resolution cube from which absorption spectra are extracted, one would need to resolve away the H I emission, while keeping as much of the continuum as possible. These are two conflicting goals, since excluding short baselines to resolve away the H I emission results in a decrease in the continuum, which in turn increases the noise in the optical depth (τ). To evaluate the impact of baseline selection, we produced three cubes with different short-spacing cut-offs: 1.055 km ($5 \text{ k}\lambda$), 316 m ($1.5 \text{ k}\lambda$), 0 (all baselines). As the beam size changes from $8.8''$ to $12.1''$ to $13.3''$, the peak continuum brightness temperature increases from 342 K to 429 K to 623 K , while the H I emission begins to leak into the cubes. Based on these results, we decided to include all baselines to extract as many absorption spectra as possible and corrected for the emission leakage later based on the average spectrum of the pixels surrounding 30 Dor (Section 2.1.5).

For our subsequent analyses, we smoothed the processed cube to $30''$ scales to match the low-resolution cube (Section 2.1.3), rebinned it with a pixel size of $12''$ for Nyquist sampling, and address the final product as the “high-resolution cube” throughout this paper. Since we did not subtract the continuum in the uv -domain, the high-resolution cube contains H I emission and absorption along with the extended continuum. To produce the continuum image, we estimated the continuum level T_{cont} from the off-line channels of 150 – 200 km s^{-1} and 320 – 380 km s^{-1} and cut out

a $7' \times 7'$ region centered on $(\alpha, \delta)_{J2000} = (05^h38^m47.9^s, -69^\circ05'56'')$ that includes all pixels where the continuum is bright enough to measure accurate H I absorption (> 83 K or $120 \text{ mJy beam}^{-1}$; Figure 2). No primary beam correction was applied, as the $7' \times 7'$ region is sufficiently small to have a correction value of unity.

2.1.3. Low-Resolution Imaging

An emission cube must be sensitive to structures on all angular scales, since a knowledge of the H I emission that arises from the absorbing gas is necessary to compute the spin temperature T_s . However, like all radio interferometers, ASKAP suffers from missing short-spacings that inherently filter out structures on angular scales larger than the maximum recoverable scale ($\sim 32'$), including the total power at $u = v = 0$.

We created an emission cube based on the imaging pipeline in N. M. Pingel et al. (2022) that utilizes WSClean, the command-line imaging package for radio data (A. R. Offringa et al. 2014). To efficiently process the ASKAP data, we imaged each spectral plane in computing jobs distributed across the resources available through the Center for High Throughput Computing at the University of Wisconsin-Madison and produced a combined cube by stitching together the deconvolved spectral planes. We used WSClean to ensure that the large-scale structures spanning across multiple ASKAP beams are accurately reconstructed through a joint-deconvolution process. In addition to the imaging parameters summarized in Table 2, we configured WSClean with *-mgain 0.7* to ensure that 70% of the residual flux is cleaned per major cycle and *-taper-gaussian 14arcsec* to convolve the cleaned image to a final resolution of $30''$. This resolution provides the best compromise between the surface brightness sensitivity to large-scale diffuse structures and the final root-mean-square (rms) noise. After deconvolution, we added the missing short-spacings by feathering the single-dish data from the Galactic All Sky Survey (GASS; N. M. McClure-Griffiths et al. 2009; P. M. W. Kalberla & U. Haud 2015) using the *feather* task in CASA. For this purpose, we set the *sdfactor* parameter to 1.0, dictating that the flux scale of the single-dish data is calibrated so that the only difference in the flux between the Parkes and ASKAP data arises from their different beam areas. We refer the readers to Section 3.2 of N. M. Pingel et al. (2022) for details on the feathering process and note that the continuum was not subtracted from the resultant low-resolution cube.

2.1.4. Extended Continuum Emission

The low-resolution cube was produced from the GASKAP and Parkes H I observations and hence contains all spatial frequencies. In contrast, the low-resolution continuum image is missing large-scale flux from the diffuse halo around 30 Dor with a diameter of $\sim 8' - 20'$, since the single-dish continuum data were not included. In our continuum image, the

diffuse halo is resolved away at radii greater than $\sim 3.5'$, probably due to a clean bowl around the bright core of 30 Dor. This suggests that the continuum brightness of 30 Dor is underestimated even in our low-resolution image and should be supplemented by an offset of $\sim 36 \text{ mJy beam}^{-1}$ to match the 1.4 GHz flux density of $31.3 \pm 1.6 \text{ Jy}$ measured by R. F. Haynes et al. (1986) with the Parkes telescope. The offset corresponds to an extra continuum brightness of 25 K for our $30''$ beam (small compared to the peak of $452 \pm 5 \text{ K}$) and was added to the low-resolution cube for subsequent analyses.

2.1.5. Leakage Spectrum in the High-Resolution Cube

The high-resolution cube filters out most of the H I emission, but not all (Section 2.1.2). To estimate the H I emission that remains in the direction of 30 Dor, we considered a set of 184 points with low continuum brightness (15 K to 40 K) in an annulus around the source center. Figure 3 shows the locations of these off-source points, as well as the median, 16th, and 84th percentiles of the distribution of the brightness temperatures in each velocity channel of the off-source spectra (residual continuum at each point subtracted from baseline fitting). Here the median off-source emission represents our estimate of the emission leakage into the high-resolution cube, while the 1σ envelope indicates the noise introduced by emission fluctuations that dominates other sources of error such as the radiometer noise (e.g., see the level of baselines at velocities below 200 km s^{-1} and above 350 km s^{-1}).

2.1.6. Absorption Spectra and Associated Uncertainties

We subtracted the leakage spectrum from all pixels in the high-resolution cube and divided the product by the continuum to calculate the absorption spectra $e^{-\tau(v)}$ toward the pixels with continuum brightness higher than 83 K . We did not consider the pixels with lower continuum brightness, since their absorption spectra are not sensitive enough to derive the emission-only spectra $T_{\text{em-only}}(v)$ (Section 2.1.7). Toward the pixels above our threshold, we also estimated the 1σ uncertainties in the measured $t = 1 - e^{-\tau(v)}$ as follows:

$$\sigma_t(v) = \frac{1}{T_{\text{cont}}} \sqrt{\sigma_n^2 + \sigma_1(v)^2} \quad (1)$$

where T_{cont} is the continuum brightness temperature, σ_n is the radiometer noise measured off-line, and $\sigma_1(v)$ is the error in the leakage spectrum.

Finally, we masked pixels that meet the following criteria and used 225 unmasked pixels for our subsequent analyses: (1) pixels with spurious negative features in $1 - e^{-\tau(v)}$ that likely result from emission fluctuations; (2) pixels where the maximum of $1 - e^{-\tau(v)}$ exceeds 0.982 ($\tau(v) > 4$); and (3) pixels with no detectable absorption (peak in $1 - e^{-\tau(v)} < 3\sigma_{\text{emt}}$; σ_{emt} = rms noise in $1 - e^{-\tau(v)}$). For the unmasked 225 pixels, the $1/\sigma_{\text{emt}}^2$ -weighted mean $1 - e^{-\tau(v)}$ spectrum and the spatial

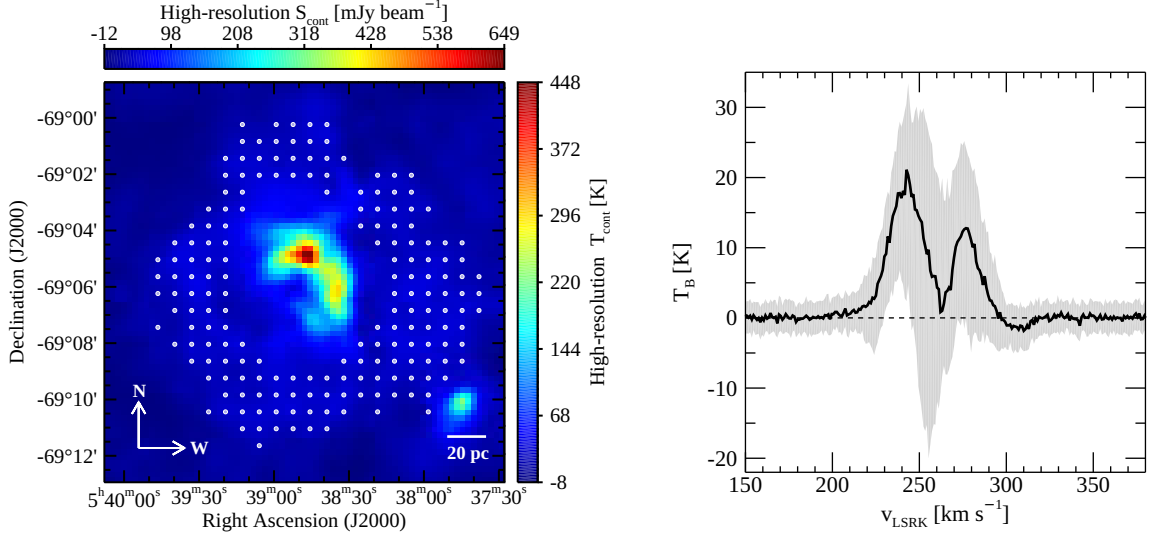


Figure 3. Derivation of the leakage spectrum. (Left) 184 off-source points that were used to derive the leakage spectrum in the high-resolution cube are shown as the white dots. The colorscale continuum image is the same as the one in Figure 2, but with a slightly larger coverage. (Right) Median of the spectra at the off-source points is shown in black, while the 1σ error computed from the distribution of the brightness temperatures in each velocity channel is indicated as the gray envelope. This error dominates the precision of our absorption and emission-only spectra.

distribution of the integrated $1 - e^{-\tau(v)}$ are shown in Figures 4 and 5.

2.1.7. Emission-only Spectra and Associated Uncertainties

The H I emission spectrum measured against a background continuum source with T_{cont} can be written as

$$T_B(v) = T_s(v)(1 - e^{-\tau(v)}) + T_{\text{cont}}e^{-\tau(v)}. \quad (2)$$

If we assume that the optical depth in each pixel of the high-resolution cube is responsible for absorbing the continuum in the corresponding pixel in the low-resolution cube, we can separate the emission and absorption and derive an emission-only cube on $30''$ scales as follows:

$$T_{\text{em-only}}(v) = T_B(v) - T_{\text{cont}}e^{-\tau(v)} \quad (3)$$

where T_{cont} and $e^{-\tau(v)}$ are measured in the low-resolution and high-resolution cubes on $30''$ scales, respectively.

Figure 6 illustrates our derivation of the emission-only spectra. The blue curve shows the absorption spectrum measured in the high-resolution cube along with the error envelope from the leakage spectrum (Section 2.1.5). The corresponding spectrum measured in the low-resolution cube is shown in green, which blends emission with absorption of the continuum of ~ 340 K. Taking this continuum times $e^{-\tau(v)}$ gives the tan curve, and subtracting this from the green curve gives the black curve at the bottom (emission-only spectrum).

In addition, we calculated the 1σ uncertainties $\sigma_o(v)$ in the emission-only spectra as follows:

$$\sigma_o(v) = \sqrt{\sigma_B^2 + \sigma_n^2 + \sigma_l(v)^2} \quad (4)$$

where σ_B is the rms noise in $T_B(v)$ as defined in Equation (2). For this calculation, we assumed that T_{cont} is measured with very low noise, which is reasonable considering that we averaged roughly 80 channels on either side of the emission line. The accuracy of T_{cont} is mainly limited by the lack of short-spacing information for the continuum (Section 2.1.4), but this does not introduce errors in the absorption and emission-only spectra.

For our subsequent analyses, we selected 225 pixels with clear detection (peak in $T_{\text{em-only}}(v) > 3\sigma_{\text{em-only}}$; $\sigma_{\text{em-only}}$ = rms noise in $T_{\text{em-only}}(v)$) and show the $1/\sigma_{\text{em-only}}^2$ -weighted mean spectrum and spatial distribution of the integrated $T_{\text{em-only}}(v)$ of these pixels in Figures 4 and 5. We note that the selected 225 pixels in the absorption and emission-only cubes¹⁹ are the same.

2.2. [C II]

To compare with H I in 30 Dor, we used the [C II] $158 \mu\text{m}$ observations from Y. Okada et al. (2019) that were obtained using SOFIA with angular and velocity resolutions of $16''$ and 1 km s^{-1} . These data were smoothed and regridded to have a resolution of $30''$ and a pixel size of $12''$ for our analyses.

2.3. $^{12}\text{CO}(2-1)$

We utilized the CO data from T. Wong et al. (2022) that were obtained with ALMA. The 12m, 7m, and total power

¹⁹ The final H I absorption and emission-only cubes, as well as their 1σ uncertainty cubes (resolution = $30''$ and pixel size = $12''$), are available online.

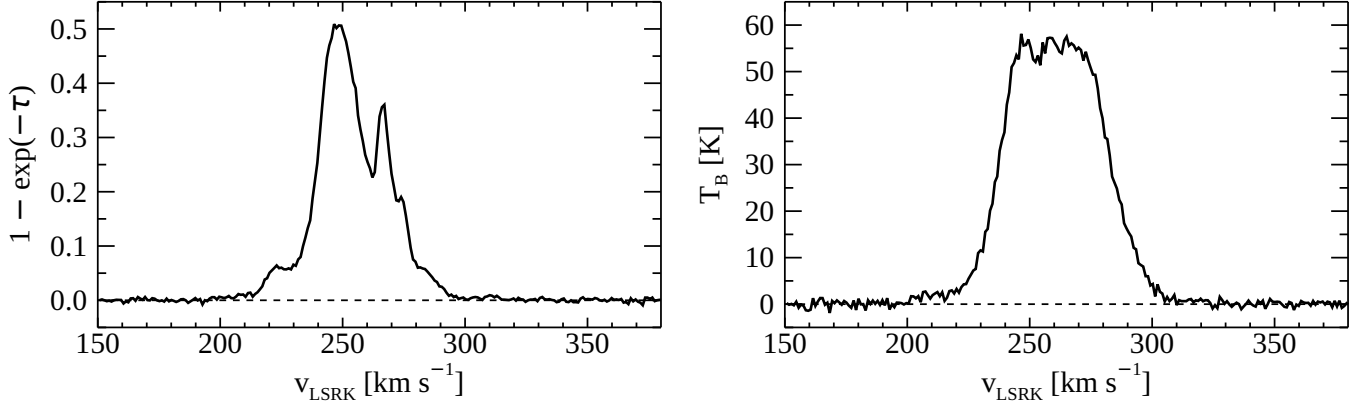


Figure 4. (Left) $1/\sigma_{\text{eml}}^2$ -weighted mean $1 - e^{-\tau(v)}$ spectrum. (Right) $1/\sigma_{\text{em-only}}^2$ -weighted mean emission-only spectrum. To produce these two spectra, the same unmasked 225 pixels in the absorption and emission-only cubes were used.

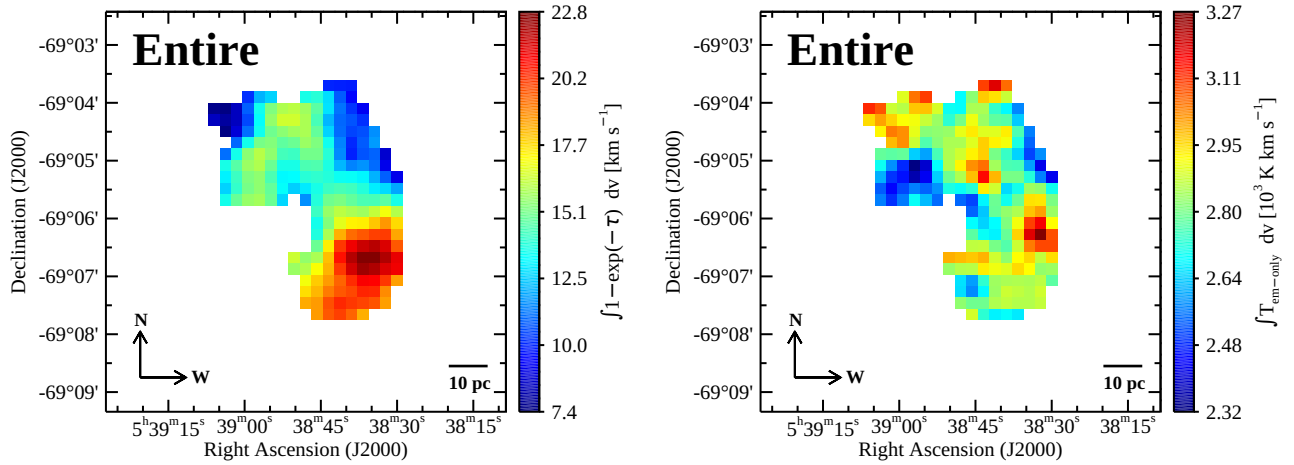


Figure 5. Spatial distributions of the integrated $1 - e^{-\tau(v)}$ (left) and $T_{\text{em-only}}$ (right). The entire velocity range of 200–300 km s^{-1} over which H I absorption and emission are clearly detected was used to produce the maps.

arrays were used for the CO observations, and the final angular and velocity resolutions were $1.8''$ and 0.3 km s^{-1} , respectively. To match our H I data, we smoothed and regridded the CO cube to have a resolution of $30''$ and a pixel size of $12''$.

3. RESULTS

In this section, we estimate various properties of the CNM (e.g., velocity, optical depth, spin temperature, etc.) and examine their global distributions.

3.1. Gaussian Decomposition of the H I Absorption Spectra

The average absorption spectrum of 30 Dor clearly shows distinct features in velocity (Figure 4). To analyze these features separately, we performed Gaussian decomposition of the high-resolution $1 - e^{-\tau(v)}$ cube. For each unmasked pixel, we started with one Gaussian and added additional components until the residuals from fitting were within $\pm\sigma_{\text{r}}(v)$. We then derived the peaks, central velocities, and full widths at half maximum (FWHMs) of the fitted Gaussian components.

Two example spectra are shown in Figure 7 to demonstrate our Gaussian decomposition, and the results for the total 225 pixels are summarized in Tables 3 and 4 and Figure 8.

We found one to six Gaussian components toward the observed LOSs, resulting in 862 in total. These components have the peak values of 0.02–0.97 in $1 - e^{-\tau}$ (median of 0.24) and FWHMs of 2.4–47.3 km s^{-1} (median of 11.4 km s^{-1}). Both parameters show approximately normal distributions with long tails beyond the peak value of ~ 0.5 and FWHM of $\sim 20 \text{ km s}^{-1}$. As for the central velocities, the fitted components are distributed at a wide range of 204–298 km s^{-1} , likely indicating the complex CNM kinematics in and around 30 Dor. To better understand the velocity distribution of the CNM components, we additionally examined how the peak values in $1 - e^{-\tau}$ change with the central velocities and found that there are largely four distinct groups with two strong peaks at $\sim 250 \text{ km s}^{-1}$ and $\sim 270 \text{ km s}^{-1}$ (Figure 9). Based on this result, we divided the entire velocity range into four bands, i.e., B1 for 200–230 km s^{-1} , B2 for 230–260 km s^{-1} ,

Table 3. Derived Gaussian Parameters for the Total 225 Pixels

| X | Y | t_{peak} | $\sigma_{t_{\text{peak}}}$ | v_0 | σ_{v_0} | FWHM | σ_{FWHM} |
|-----|-----|-------------------|----------------------------|-----------------------|-----------------------|-----------------------|------------------------|
| | | | | (km s ⁻¹) | (km s ⁻¹) | (km s ⁻¹) | (km s ⁻¹) |
| (1) | (2) | (3) | (4) | (5) | (6) | (7) | (8) |
| 9 | 25 | 0.23 | 0.01 | 253.50 | 0.59 | 33.83 | 1.56 |
| 9 | 25 | 0.05 | 0.01 | 297.53 | 2.04 | 19.64 | 4.95 |
| 9 | 26 | 0.24 | 0.01 | 258.40 | 0.60 | 33.86 | 1.52 |

NOTE—(1, 2) X and Y pixel positions in the high-resolution absorption cube; (3, 4) Peak in $1 - e^{-\tau}$ and its 1σ uncertainty; (5, 6) Central velocity and its 1σ uncertainty; (7, 8) FWHM and its 1σ uncertainty.

(This table is available in its entirety in a machine-readable form in the online journal. A portion is shown here for guidance regarding its form and content)

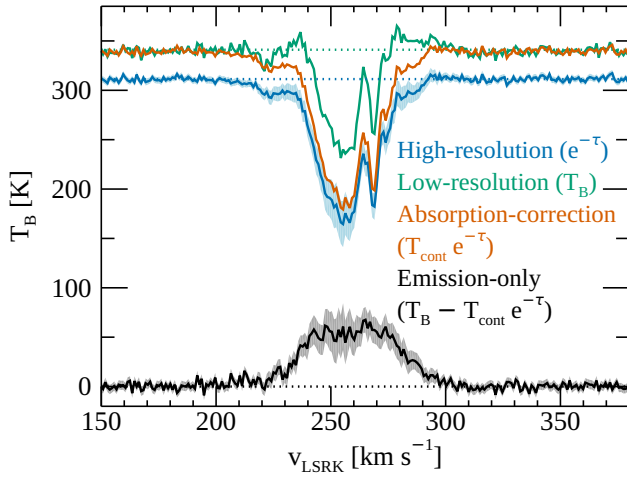


Figure 6. Derivation of the emission-only spectrum for the pixel at $(\alpha, \delta)_{J2000} = (05^{\text{h}}38^{\text{m}}45.7^{\text{s}}, -69^{\circ}05'20'')$. The blue curve shows the spectrum from the high-resolution cube along with the 1σ envelope that arises from both the radiometer noises and the uncertainties in the leakage spectrum. Dividing the blue curve by the continuum (~ 310 K) results in the absorption spectrum $e^{-\tau(v)}$. The green curve is the corresponding spectrum measured in the low-resolution cube. As described in Section 2.1.7, the tan curve is obtained by multiplying the absorption spectrum by the continuum of the green curve (~ 340 K), and subtracting the tan curve from the green curve leads to the black curve, which contains emission only. The error envelopes of the blue and black curves originate mostly from the uncertainties in the leakage spectrum.

B3 for 260–277 km s⁻¹, and B4 for 277–300 km s⁻¹, and used them for our subsequent analyses.

Since H I absorption is measured against the main H II complex at B2 velocities (Section 4.2 for details), B1, B3, and B4 are CNM structures in front of B2. In particular, we interpret B1 as outflows and B3 and B4 as inflows, considering that B1 is blueshifted (moving toward us) and B3 and B4 are redshifted (moving away from us) with respect to B2. We will revisit the nature of the CNM structures at B2 and B3 veloci-

Table 4. Global CNM Properties from Gaussian Fitting

| Property | Range | Median |
|-----------------------------|-------------|--------|
| (1) | (2) | (3) |
| t_{peak} | 0.02–0.97 | 0.24 |
| v_0 (km s ⁻¹) | 203.9–297.5 | 255.9 |
| FWHM (km s ⁻¹) | 2.4–47.3 | 11.4 |

NOTE—(1) CNM properties including the peak in $1 - e^{-\tau}$, central velocity, and FWHM; (2, 3) Range and median value.

ties in Section 4.2 and discuss the implication of the outflows and inflows for the evolution of 30 Dor in Section 5.2.

3.2. Derivation of Physical Properties

3.2.1. LOS Average Spin Temperature

In addition to the Gaussian parameters, we calculated the LOS average spin temperature $\langle T_s \rangle$ on 30'' scales, assuming an isothermal single-phase approximation as outlined by J. M. Dickey et al. (2000)

$$\langle T_s \rangle = q \frac{N(\text{H I})_{\text{unc}}}{\text{EW}} = q \frac{\int T_{\text{em-only}}(v) dv}{\int (1 - e^{-\tau(v)}) dv}, \quad (5)$$

where q is the fraction of gas in front of the continuum (e.g., $q = 1$ when all the gas is in front of the continuum), $N(\text{H I})_{\text{unc}}$ is the H I column density uncorrected for self-absorption, and EW is the equivalent width. For our calculation, we assumed a statistically probable value of $q = 0.5$ and used the entire velocity range (referred as “entire”), as well as the individual bands (B1 to B4). To ensure a reliable analysis, we estimated the 1σ uncertainties in $N(\text{H I})_{\text{unc}}$, EW, and $\langle T_s \rangle$ ($\sigma_{N(\text{H I})_{\text{unc}}}$, σ_{EW} , and $\sigma_{\langle T_s \rangle}$) by propagating the error spectra of $T_{\text{em-only}}(v)$ and $1 - e^{-\tau(v)}$ and selected the pixels that meet

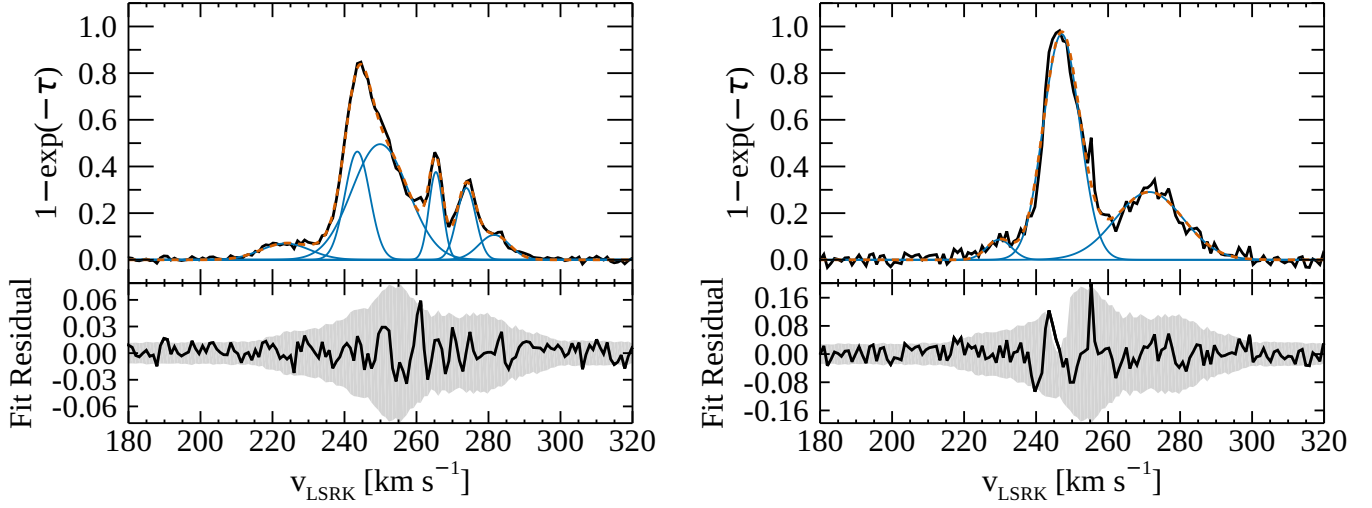


Figure 7. (Left) Absorption spectrum from the pixel at $(\alpha, \delta)_{J2000} = (05^{\text{h}}38^{\text{m}}34.4^{\text{s}}, -69^{\circ}06'20'')$. This pixel was selected to demonstrate our Gaussian fitting with the maximum number of components (six). In the top panel, the observed absorption spectrum is shown in black, while the individual components and the total fit are overlaid in blue and tan, respectively. The residuals from fitting are presented in the bottom panel along with the $\sigma_r(v)$ envelope in gray. (Right) Same as the left panel, but for the pixel with the highest value of the fitted $1 - e^{-\tau}$ (0.97) at $(\alpha, \delta)_{J2000} = (05^{\text{h}}38^{\text{m}}38.9^{\text{s}}, -69^{\circ}07'32'')$.

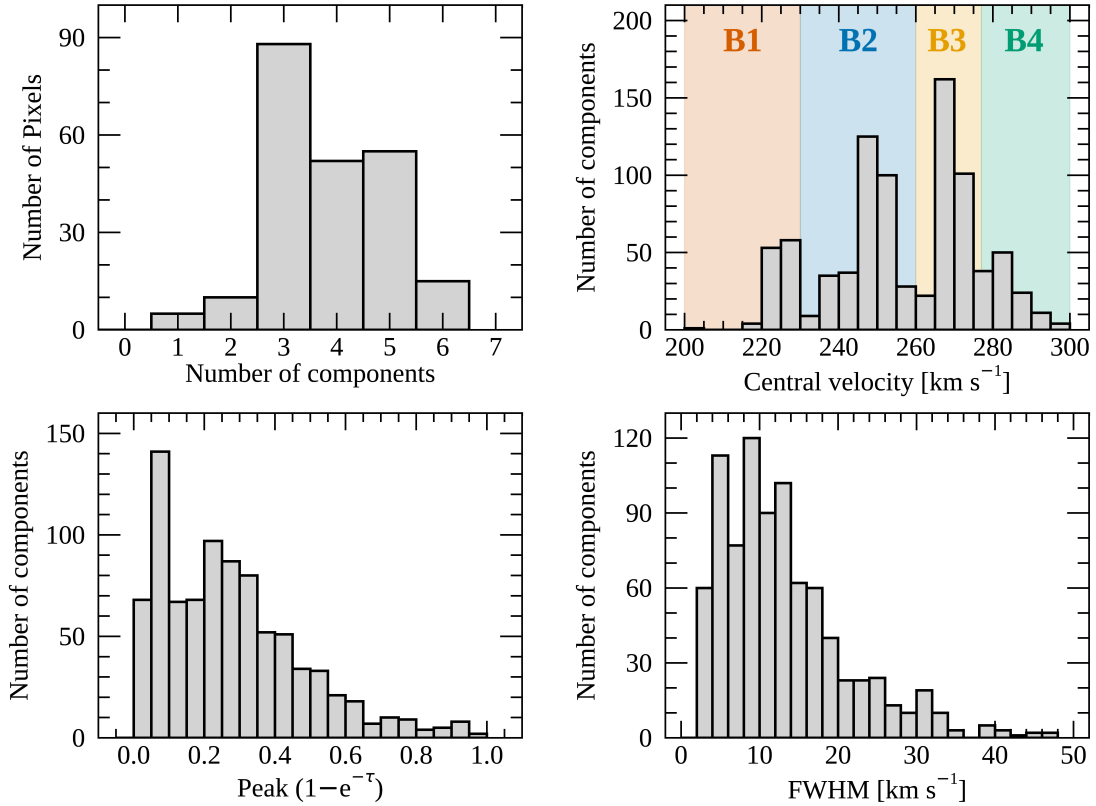


Figure 8. Histograms of the Gaussian decomposition results. (Top) Number of the fitted Gaussian components and central velocity. In the central velocity panel, the four velocity bands are shown in different colors (B1, B2, B3, and B4 in tan, blue, yellow, and green, respectively). (Bottom) Peak $1 - e^{-\tau}$ and FWHM.

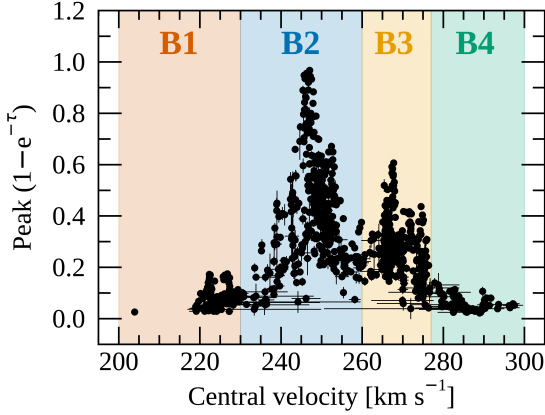


Figure 9. Peak $1 - e^{-\tau}$ as a function of the central velocity for the 862 individual Gaussian components. The four velocity bands (B1 to B4) are indicated in different colors.

$N(\text{H I})_{\text{unc}} > 3\sigma_{N(\text{H I})_{\text{unc}}}$, $\text{EW} > 3\sigma_{\text{EW}}$, and $\langle T_s \rangle > 3\sigma_{\langle T_s \rangle}$ thresholds. The calculated $\langle T_s \rangle$ values for the selected pixels are presented in Figure 10 and Table 5.

The $\langle T_s \rangle$ values for the entire velocities range from 64 K to 208 K (median of 92 K) and show roughly a Gaussian distribution with a long tail toward $\langle T_s \rangle \gtrsim 150$ K. This distribution has a small standard deviation of 27 K, suggesting that $\langle T_s \rangle$ does not change significantly on average as it is a complex quantity that depends on both T_s and a fraction of the CNM. As for the individual bands, B2 shows the coldest $\langle T_s \rangle$ distribution with a median of 70 K. B1 is slightly warmer than B2 with a median of 81 K, while having a non-negligible fraction of the pixels (13%) with exceptionally low $\langle T_s \rangle \lesssim 50$ K. Finally, B3 and B4 are systematically warmer than B1 and B2 with medians of 112 K and 201 K.

3.2.2. Opacity-corrected Total H I Column Density

To compute the opacity-corrected total H I column density for the foreground gas that is seen in absorption, we first estimated the correction factor $f_{\text{chan}}(v)$ with the one-phase approximation (each channel represents gas at a single temperature)

$$f_{\text{chan}}(v) = \frac{\tau(v)}{1 - e^{-\tau(v)}} \quad (6)$$

and applied it to the 30''-scale emission-only cube with $C = 1.823 \times 10^{18}$ and $q = 0.5$ as follows (J. M. Dickey et al. 2000):

$$N(\text{H I})_{\text{f}} (\text{cm}^{-2}) = Cq \int f_{\text{chan}}(v) T_{\text{em-only}}(v) dv \quad (\text{K km s}^{-1}). \quad (7)$$

We performed this calculation for the entire velocity range, as well as for the individual bands (B1 to B4), and selected the pixels whose $N(\text{H I})_{\text{f}}$ values are larger than the 3σ uncertainties in $N(\text{H I})_{\text{f}}$. The results for the selected pixels are summarized in Figure 11 and Table 5.

The total H I column densities calculated for the entire velocity range vary from 2.5 to $3.8 \times 10^{21} \text{ cm}^{-2}$ with a median of $3.0 \times 10^{21} \text{ cm}^{-2}$. This small variation in $N(\text{H I})_{\text{f}}$ is consistent with what J. Roman-Duval et al. (2014) found from 1'-scale H I observations of the LMC and is mainly driven by B2 and B3 whose H I abundances dominate the observed LOSs (median $N(\text{H I})_{\text{f}}$ of $(1.0\text{--}1.5) \times 10^{21} \text{ cm}^{-2}$). Similarly, B1 and B4 show a factor of two or so variation in $N(\text{H I})_{\text{f}}$, although the values are systematically lower than that for B2 (median $N(\text{H I})_{\text{f}}$ of $(1.3\text{--}4.4) \times 10^{20} \text{ cm}^{-2}$). The saturation in $N(\text{H I})_{\text{f}}$ for B1–B4 indicates the presence of H I shielding layers for H₂ formation (e.g., M.-Y. Lee et al. 2012, 2015), and we will discuss further the conditions for the H I-to-H₂ transition in 30 Dor in Section 5.1.

In addition to $N(\text{H I})_{\text{f}}$, we calculated the optically-thin H I column density along the whole LOS that includes both the foreground and background

$$N(\text{H I})_{\text{unc}} (\text{cm}^{-2}) = C \int T_{\text{em-only}}(v) dv \quad (\text{K km s}^{-1}) \quad (8)$$

using the entire velocity range and the individual bands (B1–B4). While summarizing the results in Table 5 for the pixels whose values exceed the 3σ uncertainties in $N(\text{H I})_{\text{unc}}$, we do not discuss them further since these H I column densities are not corrected for optically thick H I and are therefore lower limits on the true total H I column densities.

3.3. Comparison of Global CNM, [C II], and CO Distributions

Finally, we compared the global distribution of the CNM to [C II] and CO emission to glimpse into the environments traced by the CNM. To do so, we selected detections based on a 3σ threshold for each tracer (σ = pixel-by-pixel statistical error from off-line channels) and produced $1/\sigma^2$ -weighted average spectra for the CNM, [C II], and CO. A comparison of these average spectra is presented in Figure 12.

Figure 12 shows that the three tracers are strongest in B2, suggesting that the main dense structure in 30 Dor is located at B2 velocities. Compared to the CNM, [C II] and CO emission appear over a narrower range of velocities (B2 and B3) and share relatively simple spectral shapes. This similarity between [C II] and CO emission is consistent with what has been observed in the solar neighborhood (K. P. Hall et al. 2020).

4. ANALYSES

Our results so far suggest that the CNM structures at B1 to B4 velocities are physically distinct and trace different environments. In terms of the multi-phase structures toward 30 Dor, the CNM is overall more extended than [C II] and CO emission, probing relatively diffuse gas. In this section,

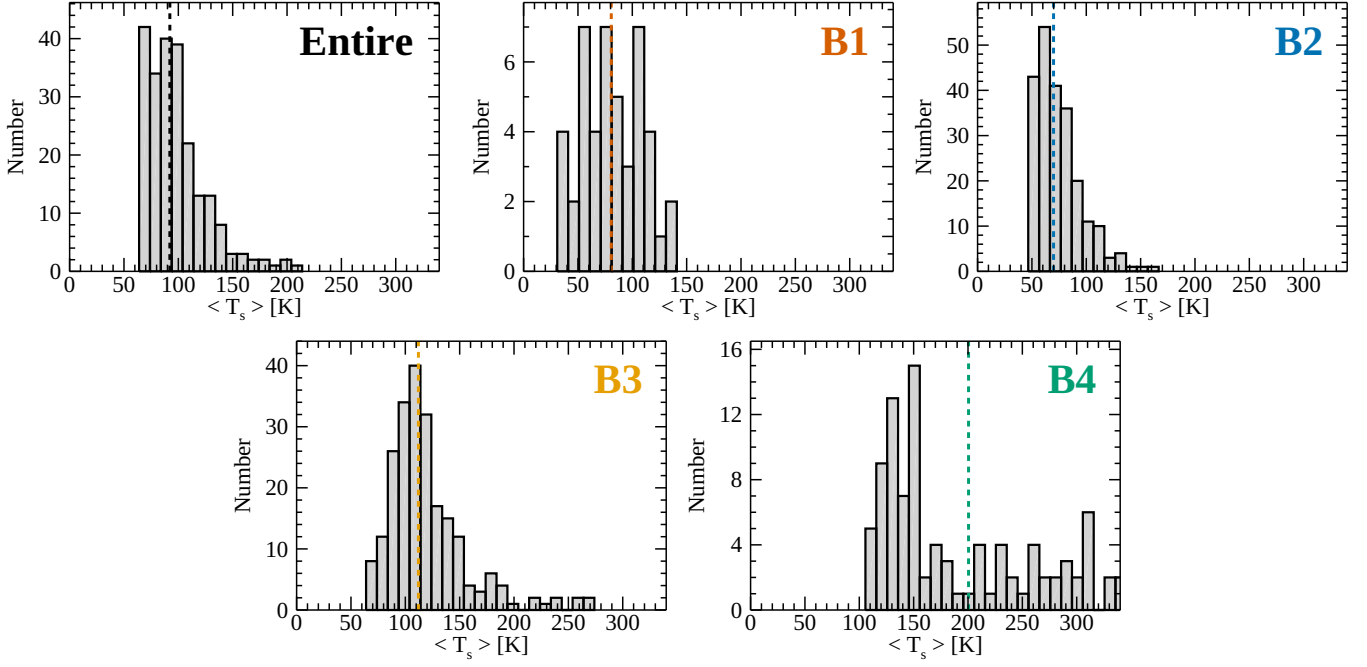


Figure 10. Histograms of the LOS average spin temperatures that were calculated for the entire velocity range (Entire) and the individual bands (B1 to B4). The median of each histogram is indicated as the dashed line.

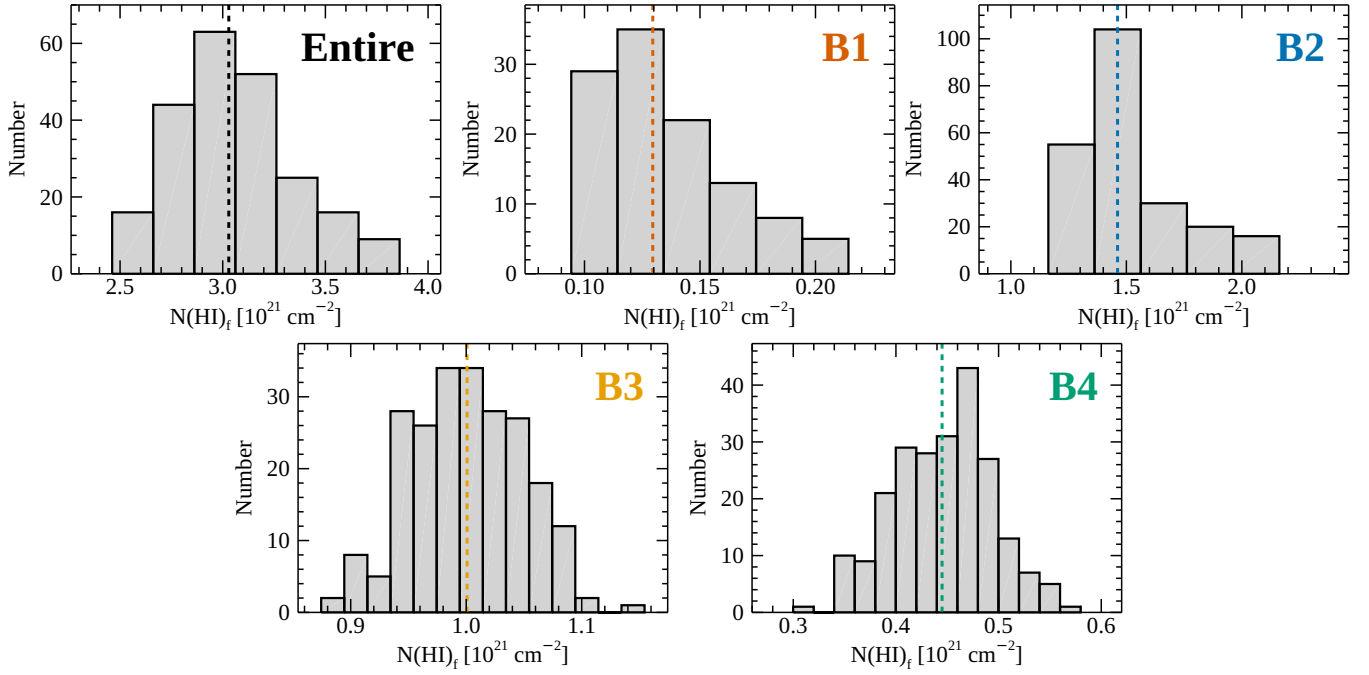


Figure 11. Same as Figure 10, but for the opacity-corrected total H I column densities.

Table 5. H I Properties at the Individual Velocity Bands

| Band | v_{LSRK} (km s ⁻¹) | # of Pixels | Fitted $1 - e^{-\tau}$ | $\langle T_s \rangle$ (K) | $N(\text{H I})_f$ (10 ²⁰ cm ⁻²) | $N(\text{H I})_{\text{junc}}$ (10 ²⁰ cm ⁻²) |
|--------|--------------------------------------------|----------------------|------------------------|------------------------------|-----------------------------------------------------------|-----------------------------------------------------------------------|
| (1) | (2) | (3) | (4) | (5) | (6) | (7) |
| B1 | 200–230 | (116, 46, 112, 109) | 0.03–0.17, 0.08 (0.01) | 31.0–138.4, 80.6 (19.1) | 0.9–2.1, 1.3 (0.3) | 1.8–4.2, 2.6 (0.6) |
| B2 | 230–260 | (225, 225, 225, 225) | 0.04–0.97, 0.39 (0.01) | 46.6–164.7, 69.9 (6.3) | 11.6–21.5, 14.6 (1.1) | 19.4–27.1, 23.4 (1.6) |
| B3 | 260–277 | (210, 223, 225, 225) | 0.04–0.61, 0.26 (0.01) | 63.9–265.5, 112.1 (11.0) | 8.7–11.3, 10.0 (0.6) | 15.3–19.5, 17.3 (1.0) |
| B4 | 277–300 | (99, 118, 225, 225) | 0.02–0.14, 0.05 (0.01) | 105.6–558.7, 200.5 (49.8) | 3.0–5.6, 4.4 (0.4) | 6.0–10.5, 8.7 (0.8) |
| Entire | 200–300 | (225, 225, 225, 225) | 0.02–0.97, 0.24 (0.01) | 63.9–207.8, 92.2 (5.6) | 24.6–38.3, 30.3 (1.3) | 42.2–59.7, 51.6 (2.2) |

NOTE—(1) Division of the velocities for our analyses; (2) Velocity range; (3) Numbers of the pixels that were used for the calculation of the peak $1 - e^{-\tau}$, $\langle T_s \rangle$, $N(\text{H I})_f$, and $N(\text{H I})_{\text{junc}}$ are presented in parentheses; (4) Peak value in the fitted $1 - e^{-\tau}$; (5) LOS average spin temperature; (6) Opacity-corrected total H I column density for the foreground gas; (7) Optically-thin H I column density for the whole LOS; (4, 5, 6, 7) Range and median value are listed. The number in each parentheses corresponds to the median value in the 1σ uncertainties. (5, 6) $q = 0.5$ was adopted.

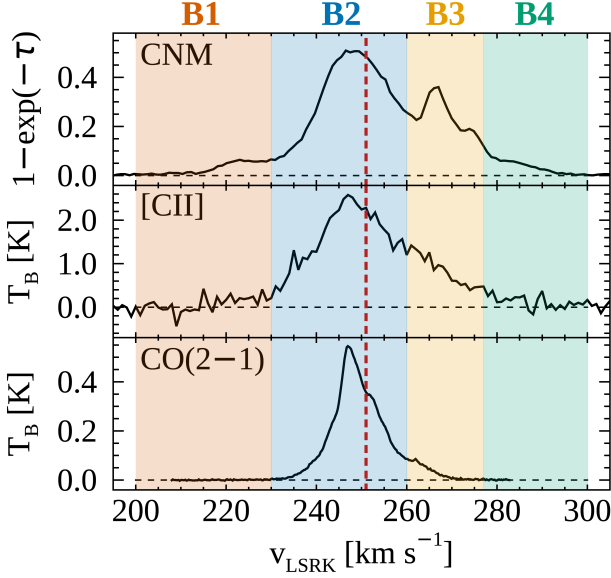


Figure 12. Comparison of the $1/\sigma^2$ -weighted average CNM, [C II], and CO spectra (30'' scales). The four velocity bands are indicated in different colors, and the central velocity of H α emission is marked as the red dashed line (Section 4.2).

we will analyze closely the observed properties of the CNM along with supplementary data to investigate how the CNM changes in different environments.

4.1. Spatial Distributions of the CNM Properties

First, we probed the spatial distributions of the CNM properties that were calculated for the entire velocity range, as well as for the B1–B4 bands (Figures 13, 14, and 15). For the three properties in our examination, peak $1 - e^{-\tau}$, $\langle T_s \rangle$, and $N(\text{H I})_f$, we found that the distributions for the entire velocity range resemble those for B2, hinting that the CNM structures at B2 velocities are the most prominent in 30 Dor. In the following discussions, we focus on the comparison between the B1–B4 distributions.

For B2 and B3, the absorption is detected over almost the entire region of the strong continuum, with the peak $1 - e^{-\tau}$ changing significantly from 0.04 to 0.97 for B2 and from 0.04 to 0.61 for B3. In terms of the spatial distribution, B2 shows the highest optical depths in the south at $(\alpha, \delta)_{\text{J2000}} \sim (05^{\text{h}}38^{\text{m}}39^{\text{s}}, -69^{\circ}07'32'')$, while $1 - e^{-\tau} < 0.7$ in the north at $\delta > -69^{\circ}06'$. On the other hand, B3 has the highest $1 - e^{-\tau}$ values in the northeastern region at $(\alpha, \delta)_{\text{J2000}} \sim (05^{\text{h}}39^{\text{m}}01^{\text{s}}, -69^{\circ}05'20'')$. The rest of B3 shows moderate absorption with $1 - e^{-\tau} \sim 0.3$, with a few spots where $1 - e^{-\tau}$ reaches 0.5, e.g., $(\alpha, \delta)_{\text{J2000}} \sim (05^{\text{h}}38^{\text{m}}41^{\text{s}}, -69^{\circ}05'44'')$. In contrast to B2 and B3, the absorption is only partially detected for B1 and B4 with much less strength. Specifically, B1 shows mostly $1 - e^{-\tau} < 0.1$, except for two spots at $(\alpha, \delta)_{\text{J2000}} \sim (05^{\text{h}}38^{\text{m}}43^{\text{s}}, -69^{\circ}04'56'')$ and $(05^{\text{h}}38^{\text{m}}41^{\text{s}}, -69^{\circ}06'44'')$ where $1 - e^{-\tau} \sim 0.17$. In

Table 6. [C II] and CO Properties at B2 and B3 Velocities

| Band | # of Pixels | $W([\text{C II}])$ (K km s $^{-1}$) | $W(\text{CO})$ (K km s $^{-1}$) |
|------|-------------|--------------------------------------|----------------------------------|
| (1) | (2) | (3) | (4) |
| B2 | (376, 675) | −4.9, 226.9, 33.8 | 0.1, 40.5, 2.0 |
| B3 | (376, 675) | −7.4, 63.9, 10.5 | 0.0, 3.6, 0.3 |

NOTE—(1) Velocity band; (2) Numbers of the detected pixels that were considered for the $W([\text{C II}])$ and $W(\text{CO})$ statistics are presented in parentheses; (3, 4) Minimum, maximum, and median values are summarized.

B4, the absorption is primarily detected in the north at $\delta > -69^{\circ}05'40''$ with $1 - e^{-\tau} \sim 0.02$ –0.1, except for a spot at $(\alpha, \delta)_{\text{J2000}} \sim (05^{\text{h}}38^{\text{m}}34^{\text{s}}, -69^{\circ}06'32'')$ where $1 - e^{-\tau} \sim 0.14$.

The above-mentioned structure in absorption mainly determines the distributions of the spin temperature and opacity-corrected total H I column density, since the emission varies much more smoothly than the absorption. In general, B2 has lower spin temperatures than B3, i.e., $\langle T_s \rangle$ primarily in the range of 50–75 K for B2 and 70–120 K for B3. Both B2 and B3 reveal higher spin temperatures along the northern edge of the continuum at $(\alpha, \delta)_{\text{J2000}} \sim (05^{\text{h}}39^{\text{m}}04^{\text{s}}, -69^{\circ}04'20'')$, with $\langle T_s \rangle$ reaching 165 K and 265 K for B2 and B3, respectively. Compared to B3, B1 and B4 have systematically lower and higher spin temperatures. For example, while $\langle T_s \rangle$ is measured only for a handful number of pixels, it mostly ranges from 30 K to 80 K for B1. On the other hand, $\langle T_s \rangle$ changes from 106 K to 559 K for B4, with the lowest values in the south at $\delta < -69^{\circ}06'15''$. Interestingly, the lowest and highest spin temperatures for B1 and B4 are found around the continuum peak, implying that the expanding H II region somehow plays a role in the heating and cooling of the cold H I.

In terms of the opacity-corrected H I column density, B2 is the most dominant structure with $N(\text{H I})_f$ increasing from 1.2 to $2.2 \times 10^{21} \text{ cm}^{-2}$ toward the south at $\delta < -69^{\circ}06'$. In B3, the H I column density distribution becomes much more uniform with $N(\text{H I})_f \sim (0.9\text{--}1.1) \times 10^{21} \text{ cm}^{-2}$, and its highest value is found in a small region at $(\alpha, \delta)_{\text{J2000}} \sim (05^{\text{h}}38^{\text{m}}46^{\text{s}}, -69^{\circ}05'08'')$ that corresponds to the peak of the continuum. The remaining B1 and B4 have systematically lower H I column densities than B2 and B3. Specifically, B4 shows about half the H I column density of B3, i.e., $N(\text{H I})_f \sim (0.3\text{--}0.6) \times 10^{21} \text{ cm}^{-2}$, with the higher values in the south at $\delta < -69^{\circ}06'$. Similarly, B1 shows low H I column densities of $(0.1\text{--}0.2) \times 10^{21} \text{ cm}^{-2}$ for a small number of pixels. The spatial coverage for B1 is limited mainly because B1 is weak in both emission and absorption.

4.2. Multi-phase Structures in and around 30 Dor

To understand the context of the observed CNM structures, we examined the spatial distributions of multi-phase tracers in and around 30 Dor. For our examination, we focused on B2 and B3 and compared the H I, [C II], and CO distributions along with the 1.4 GHz continuum (tracing the H II region). To derive the [C II] and CO distributions for B2 and B3, we computed the integrated intensities, $W([C II])$ and $W(CO)$, by integrating the data cubes over the corresponding velocity ranges. The comparison of the individual tracers is presented in Figure 16 and Table 6.

We first start our discussion from B2. Given that H α emission peaks at 251 km s⁻¹ in 30 Dor (266 km s⁻¹ in the heliocentric frame; Y.-H. Chu & R. C. Kennicutt 1994), we probe the structures associated with the main H II complex at B2 velocities. These structures are strong in H I, CO, and [C II] as well (Section 3.3). When examined closely, H I, CO, [C II], and 1.4 GHz continuum show largely two structures in the north and south. CO, [C II], and 1.4 GHz continuum are strongest in the north, and the CO and [C II] peaks are slightly offset from the 1.4 GHz continuum peak. On the other hand, the H I peak surrounds the weaker CO and [C II] clumps in the south. These differences between the northern and southern structures in terms of the relative strengths in the ionized, atomic, and molecular gas tracers likely result from the variations in local conditions, such as the gas density and strength of UV radiation (e.g., M. Chevance et al. 2016).

The multi-phase structures at B3 velocities are drastically different from those at B2 velocities. For example, the H I and 1.4 GHz continuum distributions do not have much similarity, except that their peaks coincide well. In addition, CO and [C II] show overall two structures in the west and east, which tend to surround multiple H I clumps. While both B3 and B4 are inflows, B3 is systematically colder and denser than B4, as evidenced by the lower spin temperatures and higher H I column densities (Section 3.2.1), as well as by the presence of CO and [C II] emission. This suggests that B3 may be able to fuel star formation in 30 Dor and possibly has a different origin compared to B4 (Section 5.2 for details).

4.3. Comparison to the Milky Way and the LMC

Finally, we compared the observed properties of H I in 30 Dor to those in the Milky Way and the LMC to examine how H I changes in different environments. For the comparison to the Milky Way, we selected the 21-SPONGE (C. E. Murray et al. 2018) and GNOMES (S. Stanimirović et al. 2014; H. Nguyen et al. 2019) surveys and calculated $\langle T_s \rangle$ and $N(H I)$ by applying Equations (5), (6), and (7) to the published H I emission and absorption spectra with $q = 1$ (appropriate since their background sources are extragalactic). These two surveys are distinctly different: 21-SPONGE probes mostly diffuse environments at high and intermediate latitudes with

an exceptional optical depth sensitivity of $\sigma_\tau < 10^{-3}$, while GNOMES focuses on the surroundings of MCs where total column densities are relatively high. To follow the measurements for the Milky Way as much as possible, we used the peak $1 - e^{-\tau}$ values of the individual Gaussian components, as well as the $\langle T_s \rangle$ and $N(H I)_f$ values that were estimated for the entire velocity range with $q = 0.5$, for 30 Dor. The histograms of the peak $1 - e^{-\tau}$, LOS average spin temperature, and opacity-corrected total H I column density are presented in Figure 17.

A comparison of the 21-SPONGE and GNOMES distributions shows that they are distinctly different even for the same latitude ranges, implying that the region of interest and sensitivity of a survey affect the observed properties of H I. With this caveat in mind, we conclude that H I in 30 Dor is dissimilar from that in the Milky Way at high latitudes ($|b| > 5^\circ$) in a way that the LOS average spin temperature is systematically lower and the total H I column density is higher. The LOS average spin temperature in 30 Dor is still lower when it is compared to that in the Milky Way at low latitudes ($|b| < 5^\circ$).

In addition to the Milky Way, we compared our 30 Dor observations to the latest survey of H I absorption in the LMC by Liu et al. (2025, in preparation; L25 hereafter). L25 measured H I absorption toward 92 extragalactic background sources with the Australia Telescope Compact Array (ATCA) and calculated $\langle T_s \rangle$ and $N(H I)$ for all LOSs by applying Equations (5), (6), and (7) with $q = 1$ to their absorption spectra and the emission data from S. Kim et al. (1999). A qualitative comparison shows lower LOS average spin temperatures and higher total H I column densities in our observations than the L25 LOSs that are located far away from 30 Dor (angular separation $> 1^\circ$). For a small number of L25 LOSs closer to 30 Dor, on the other hand, the LOS average spin temperature is comparable and the optical depth is higher compared to what we measured.

In summary, we found that H I in 30 Dor is distinctly different from that in the high-latitude Milky Way, as well as from that in the less star-forming part of the LMC, with lower LOS average spin temperatures and higher total H I column densities. The lower LOS average spin temperatures suggest an intrinsically colder temperature of the CNM and/or a higher fraction of the CNM in 30 Dor. According to the theoretical model by S. Bialy & A. Sternberg (2019), the density and fraction of the CNM increases, as the thermal pressure increases in a half-solar metallicity environment. Our approximate derivation of the thermal pressure based on the H I, [C II], and dust data indeed revealed that 30 Dor and its surrounding region have thermal pressures of $(0.7\text{--}36.7) \times 10^4 \text{ cm}^{-3} \text{ K}$ (Appendix A), which are systematically higher than solar neighborhood values (e.g. E. B. Jenkins & T. M. Tripp 2011; P. F. Goldsmith et al. 2018). Higher CNM fractions may be symptomatic of starburst conditions, as the

H I observations of the Galactic mini-starburst region W43 also hinted (S. Bihr et al. 2015).

5. DISCUSSION

5.1. H I-to-H₂ Transition in 30 Dor

In Section 3.2.2, we showed that the H I column densities at B1–B4 velocities change by a factor of two or so only across ~60 pc scale regions. Considering that our $N(\text{H I})$ estimates are corrected for high optical depth, this result strongly indicates the presence of H I shielding layers in 30 Dor. Steady-state H₂ formation models have predicted such layers in star-forming regions where a certain amount of H I column density is required to shield H₂ against dissociating UV photons. For example, A. Sternberg et al. (2014) formulated an analytic model of the H I-to-H₂ transition in a one-dimensional plane-parallel slab of gas and predicted the total H I column density for one-sided beamed UV radiation as

$$N(\text{H I}) (\text{cm}^{-2}) = \frac{5.3 \times 10^{20}}{Z' \phi_g} \ln \left(\frac{\alpha G}{2} + 1 \right) \quad (9)$$

where Z' is the metallicity relative to the solar value, and ϕ_g is the order unity grain composition factor. Here one-sided irradiation by a beam radiation field is adopted, considering that the H I column densities were measured for foreground structures that are primarily illuminated by R136 (e.g., M. Chevance et al. 2016; M. Y. Lee et al. 2019).

For the dimensionless parameter αG , S. Bialy & A. Sternberg (2016) provided the following formula based on an updated expression of the total H₂-dust-limited effective dissociation bandwidth:

$$\alpha G = 0.59 I_{\text{UV}} \left(\frac{100 \text{ cm}^{-3}}{n} \right) \left(\frac{9.9}{1 + 8.9 \phi_g Z'} \right)^{0.37} \quad (10)$$

where I_{UV} is the strength of UV radiation normalized to the Draine field (B. T. Draine 1978; S. Bialy 2020), and n is the total gas number density.

Equation 9 shows that αG solely determines the total H I column density at the H I-to-H₂ transition point for given environmental conditions (Z' and ϕ_g). The dimensionless parameter αG has the physical meaning of the ratio of the effective H₂ photodissociation rate (accounting for UV shielding) to the H₂ formation rate and can range from small to large values. For example, when $\alpha G \ll 1$ (“weak-field limit”), H₂ self-shielding is mainly responsible for the absorption of dissociating UV photons and results in a gradual H I-to-H₂ transition where most of the H I column density is accumulated past the transition point. On the other hand, when $\alpha G \gtrsim 1$ (“strong-field limit”), dust absorption becomes dominant and makes the H I-to-H₂ transition sharp due to the exponential reduction of UV photons. In this case, the H I column density is primarily built up prior the transition point, producing distinct H I shielding layers.

When $Z' = 0.5$ and $\phi_g = 1$ are assumed, the measured H I column densities of $(1.3\text{--}14.6) \times 10^{20} \text{ cm}^{-2}$ at B1–B4 velocities (median values in Table 5) correspond to $\alpha G \sim 0.3\text{--}5.9$. An interesting region to compare with is the low-mass star-forming complex in the solar neighborhood, Perseus, where $\alpha G \sim 5\text{--}26$ was estimated (S. Bialy et al. 2015). Perseus is significantly different from 30 Dor in terms of environmental conditions (e.g., solar metallicity, weak UV radiation of 1–2 Draine fields, and low thermal pressure of a few $\times 10^3 \text{ cm}^{-3} \text{ K}$; M.-Y. Lee et al. 2012; P. F. Goldsmith et al. 2018) and H I properties (e.g., low CNM fraction of 0.3; S. Stanimirović et al. 2014). Yet Perseus and 30 Dor are comparable as to the nature of the H I-to-H₂ transition (“strong-field limit”). This could be because dust grains, the site for H₂ formation and the primary source for the reduction of UV photons, play a key role in the H I-to-H₂ transition over a wide range of environmental conditions and the decrease of metallicity in 30 Dor is not so significant as to change the nature of the H I-to-H₂ transition. Perhaps the most surprising result from our analysis would be that H I shielding layers predicted by simple steady-state H₂ formation models exist in extreme environments like 30 Dor where various energetic processes (e.g., stellar outflows and winds and expanding H II regions) constantly influence the surrounding ISM. We will revisit the H I-to-H₂ transition in and around 30 Dor in our forthcoming paper, confronting the model by A. Sternberg et al. (2014) more rigorously with the observed ISM properties (e.g., I_{UV} , n , and ϕ_g).

5.2. Outflows and Inflows

As discussed in Section 3.1, we interpret B1 as outflows and B3 and B4 as inflows. To derive the outflow and inflow rates \dot{M}_{outflow} and \dot{M}_{inflow} , we assumed spherically symmetric flows that are moving at a constant radial velocity of δv_r with a covering factor of f_c . These flows start from the surface of the H II region whose radius is R , and the density decreases radially as $1/r^2$. The mass flux rate \dot{M} can then be calculated as

$$\begin{aligned} \dot{M} (M_{\odot} \text{ yr}^{-1}) &= 4\pi \mu m_{\text{H}} f_c \delta v_r R N(\text{H I}) \\ &= 1.4 \times 10^{-5} f_c \left(\frac{\delta v_r}{\text{km s}^{-1}} \right) \left(\frac{R}{\text{pc}} \right) \left(\frac{N(\text{H I})}{10^{20} \text{ cm}^{-2}} \right) \end{aligned} \quad (11)$$

where $\mu = 1.4$ is the average particle mass in units of the hydrogen mass m_{H} , f_c is the covering factor, δv_r is the relative radial velocity of the flow with respect to the H II region, R is the radius of the H II region, and $N(\text{H I})$ is the H I column density that is measured up to the H II region. For our calculation, we adopted $f_c = 0.5$ for B1 and $f_c = 1$ for B3 and B4, based on the covering fraction of H I in Figure 15, and $\delta v_r = -25 \text{ km s}^{-1}$, 18 km s^{-1} , and 34 km s^{-1} for B1, B3, and

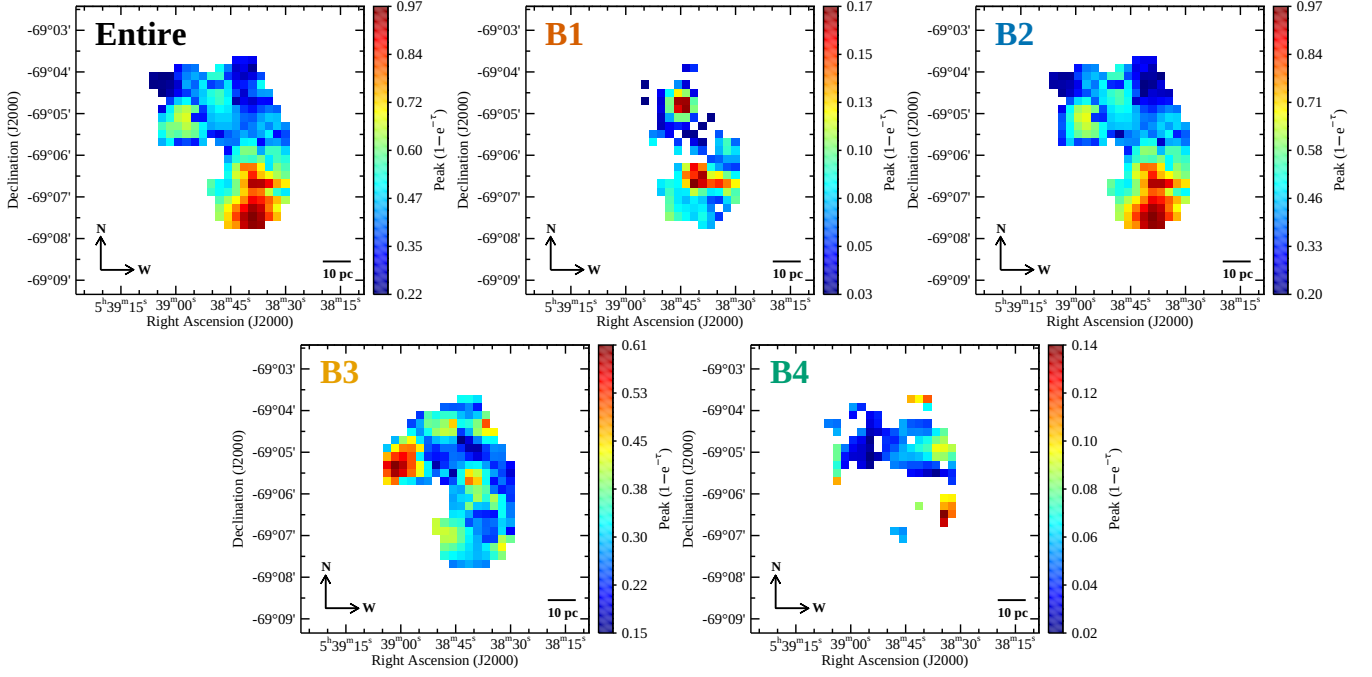


Figure 13. Spatial distributions of the peak $1 - e^{-\tau}$ values for the entire velocity range (Entire) and the individual bands (B1 to B4). The angular resolution of these maps is $30''$.

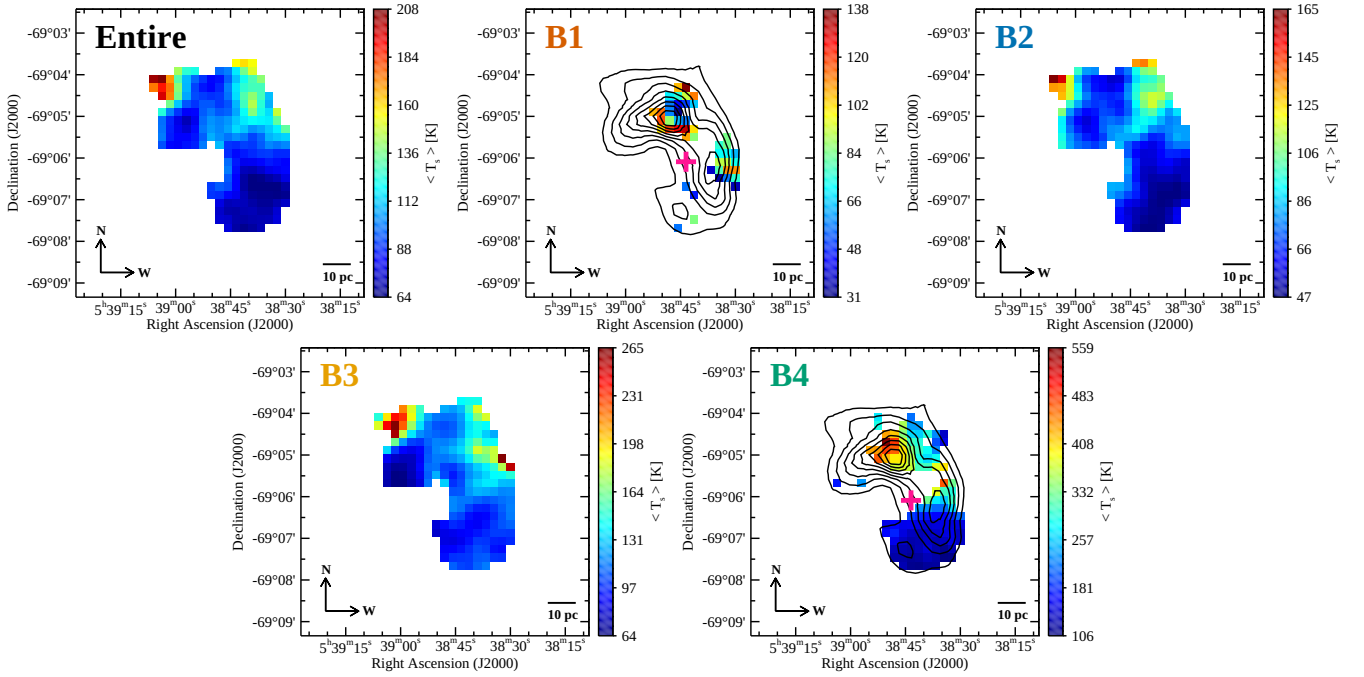


Figure 14. Same as Figure 13, but for $\langle T_s \rangle$. For B1 and B4, the 1.4 GHz continuum data from the high-resolution cube are overlaid as the contours with levels ranging from 20% to 90% of the peak value (448 K) in steps of 10%. The location of R136 is indicated as the red cross.

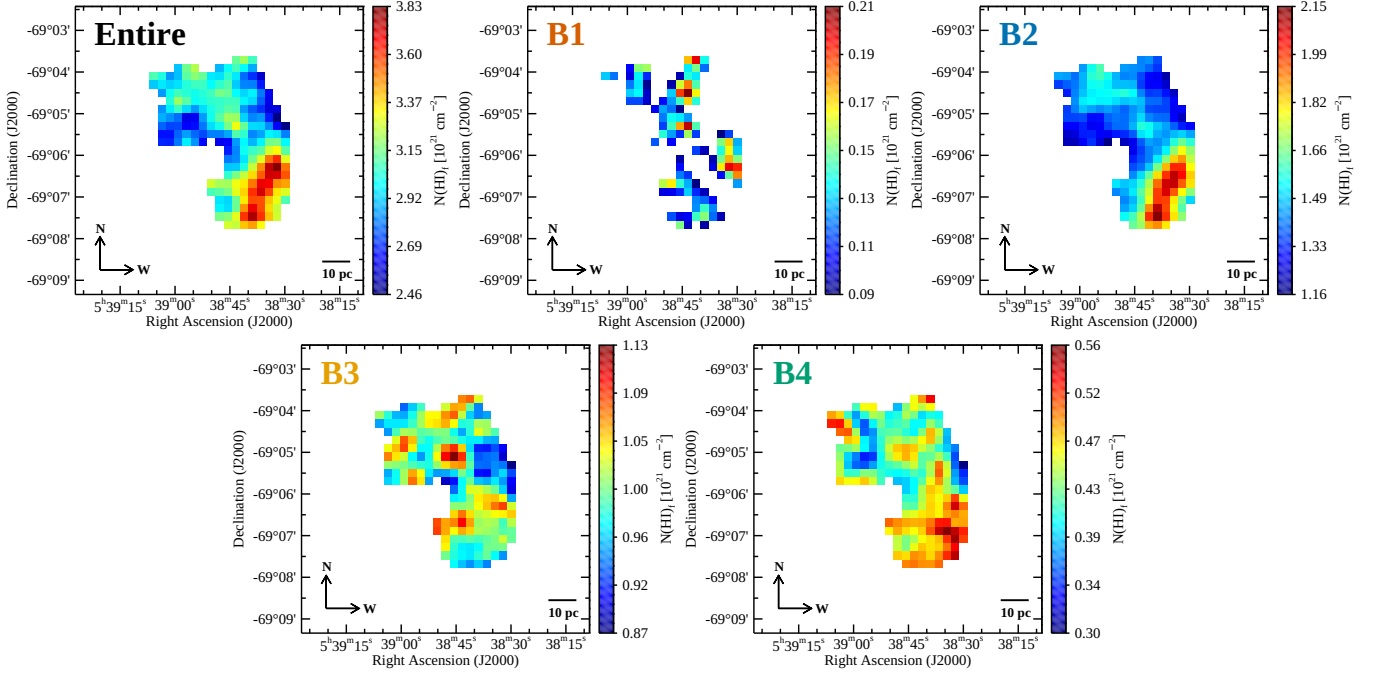


Figure 15. Same as Figure 13, but for $N(\text{H I})_f$.

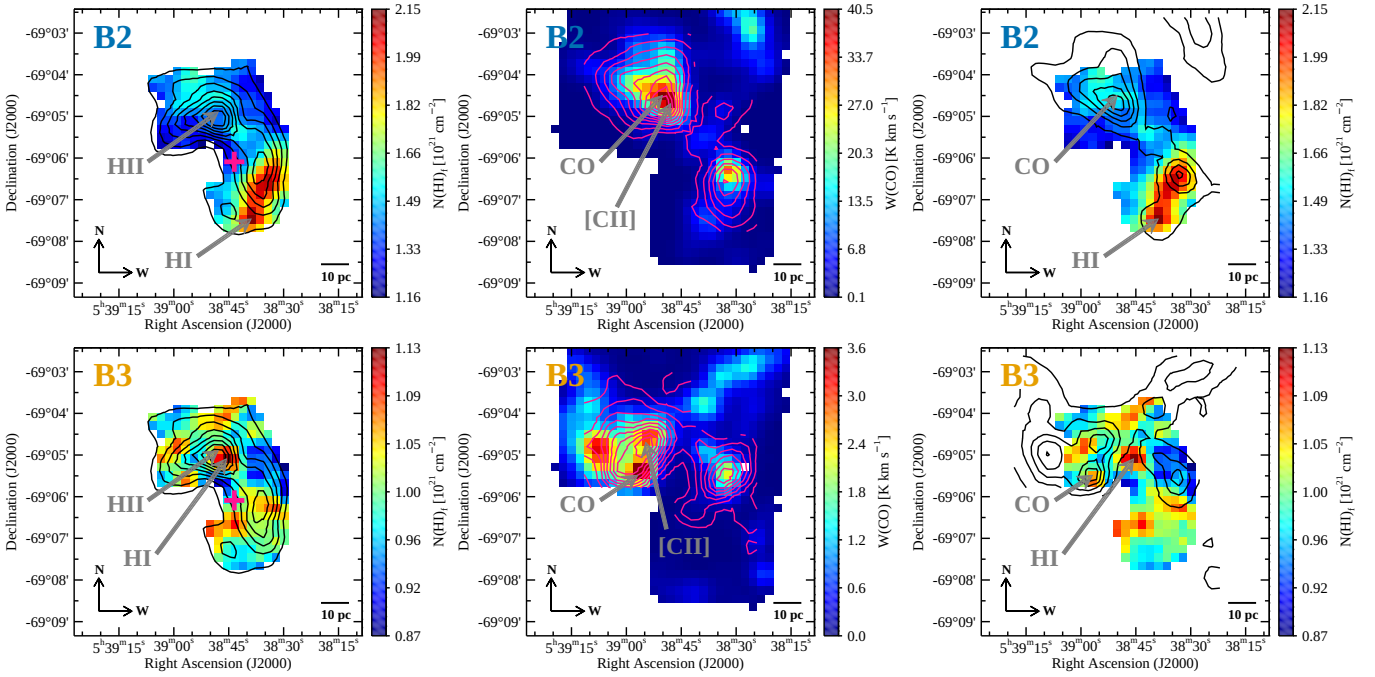


Figure 16. Comparison of the multi-phase tracers for B2 and B3 (all tracers on $30''$ scales). The colorscale images show $N(\text{H I})_f$ in the left and right panels and $W(\text{CO})$ in the middle panel. The 1.4 GHz continuum data are overlaid as the contours in the left panel with levels ranging from 20% to 90% of the peak value (448 K) in 10% steps. Similarly, $W([\text{C II}])$ and $W(\text{CO})$ are shown as the contours in the middle and right panels, respectively, with levels ranging from 10% to 90% of the peak values in 10% steps for $[\text{C II}]$ and 20% steps for CO. The peak values are 227 K km s^{-1} and 64 K km s^{-1} for $[\text{C II}]$ in B2 and B3, respectively, and 40 K km s^{-1} and 4 K km s^{-1} for CO in B2 and B3, respectively. The location of R136 is shown as the red cross, and the peak of each tracer is indicated with the grey arrow.

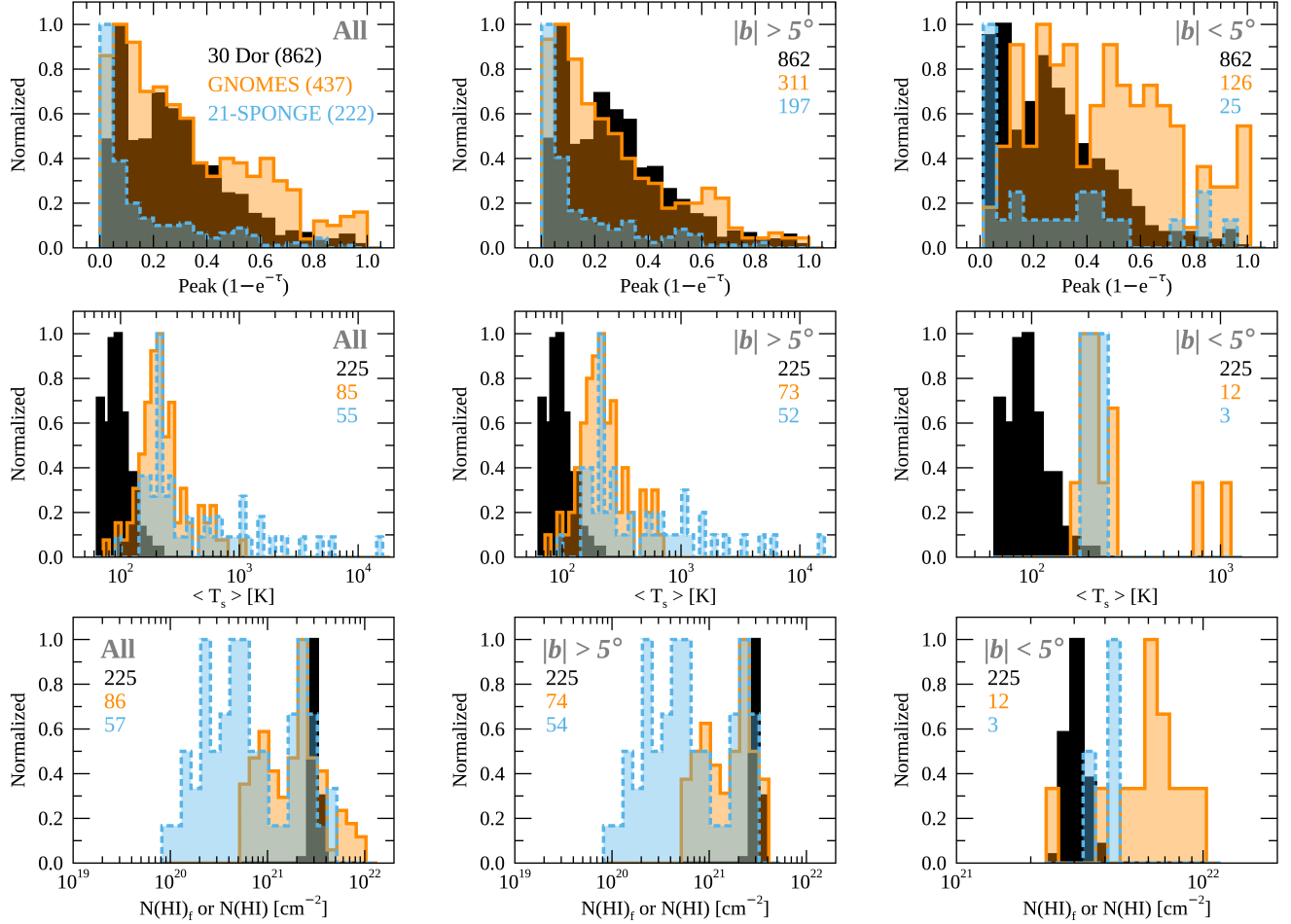


Figure 17. Normalized histograms of the peak $1 - e^{-\tau}$ (top), $\langle T_s \rangle$ (middle), and $N(\text{H I})_f/N(\text{H I})$ (bottom) from the 21-SPONGE, GNOMES, and 30 Dor observations. The values of the individual Gaussian components were used for the peak $1 - e^{-\tau}$, while those of the entire velocities were employed for $\langle T_s \rangle$, $N(\text{H I})_f$, and $N(\text{H I})$. Different q values of 0.5 and 1 were adopted for 30 Dor and the Milky Way, respectively, and the $N(\text{H I})$ histograms hence show $N(\text{H I})_f$ for 30 Dor (foreground) and $N(\text{H I})$ for the Milky Way (all gas along the observed LOSs). We note that $N(\text{H I})_f$ for 30 Dor is a lower limit on the total H I column density along the whole LOSs, since it includes the foreground gas only. Finally, the numbers of the Gaussian components and LOSs considered for the histograms are indicated in sky blue, orange, and black, respectively. (Left) Entire population of the observed LOSs is included for the comparison. (Middle) LOSs at $|b| > 5^\circ$ for the Milky Way are selected to compare with the 30 Dor results. (Right) Same as the middle panel, but with the LOSs at $|b| < 5^\circ$ for the Milky Way.

B4, respectively, where we took δv_r to be the median central velocity of the fitted Gaussians minus the H II region velocity of 251 km s^{-1} . In addition, we used $N(\text{H I}) = 1.3 \times 10^{20} \text{ cm}^{-2}$, $1.0 \times 10^{21} \text{ cm}^{-2}$, and $4.4 \times 10^{20} \text{ cm}^{-2}$ (median H I column densities) for B1, B3, and B4, respectively, as well as $R = 2'$ or 30 pc.

While keeping in mind that our estimates are approximate based on simplified spherical flows for the front side only and could change depending on the actual geometry that is currently unknown (e.g., biconic flows), we measured $\dot{M}_{\text{outflow}} = 0.007 M_\odot \text{ yr}^{-1}$ for B1 and $\dot{M}_{\text{inflow}} = 0.08 M_\odot \text{ yr}^{-1}$ and $0.06 M_\odot \text{ yr}^{-1}$ for B3 and B4, respectively. The total inflow rate of $0.14 M_\odot \text{ yr}^{-1}$ is comparable to the star formation rate of $0.18 M_\odot \text{ yr}^{-1}$ that was estimated by O. Nayak et al. (2023) based on the number of young stellar objects (YSOs), suggesting that the accreted atomic gas could sustain star for-

mation in 30 Dor. The outflow rate, on the other hand, is only 5% of the total inflow rate.

Recently, S. Poudel et al. (2025) analyzed ULLYSES UV absorption spectra toward eight LOSs probing 30 Dor and its surrounding region and found blueshifted absorption components at $150\text{--}230 \text{ km s}^{-1}$ in atomic ($\text{O I } \lambda 1302$) and ionized ($\text{Si II } \lambda 1526$, $\text{Fe II } \lambda 2344$, $\text{C IV } \lambda 1550$, etc.) gas tracers. B1 lies within the observed velocities of these absorption components, suggesting that B1 is associated with large-scale outflows driven by active star formation in 30 Dor. In terms of mass, the H I outflow rate of $0.007 M_\odot \text{ yr}^{-1}$ is a fraction of the ionized outflow rate of $\gtrsim 0.02 M_\odot \text{ yr}^{-1}$. One of the interesting features about B1 is that it is exceedingly weak in H I emission (e.g., Figure 4). This implies that the observed outflows consist of ionized gas along with the CNM and very little of the WNM. As discussed in Section 4.3,

the high fraction of the CNM could result from high thermal pressures. For example, the WNM no longer exists at thermal pressures higher than $10^4 \text{ cm}^{-3} \text{ K}$ in the solar neighborhood condition (S. Bialy & A. Sternberg 2019). While it is currently unclear exactly how stellar activities drive the observed outflows, high thermal pressures are expected from various radiative and mechanical feedback processes related to star formation in 30 Dor, e.g., strong UV radiation, stellar outflows and winds, etc. The thermal pressure of $(2.6\text{--}20.7) \times 10^4 \text{ cm}^{-3} \text{ K}$ for B1 is indeed systematically higher than the solar neighborhood (e.g., E. B. Jenkins & T. M. Tripp 2011; P. F. Goldsmith et al. 2018), as well as B3 and B4 (Appendix A).

In addition to the blueshifted absorption, S. Poudel et al. (2025) found redshifted absorption from 290 km s^{-1} to 320 km s^{-1} toward six of the eight LOSs. Considering that B4 is seen in H I emission and absorption, the S. Poudel et al. (2025) result suggests that the observed inflows consist of the CNM, WNM, and ionized gas. These multi-phase inflows have different properties compared to the outflows, i.e., lower thermal pressures (so that the CNM and WNM can co-exist), higher LOS average spin temperatures, and higher H I column densities (Section 3.2). As for the origin of the inflows, S. Poudel et al. (2025) suggested that the redshifted absorbers might represent inflowing materials that are recycling back from the outflows. Or the inflows could be produced by the tidal interaction between the LMC and SMC (e.g., K. A. G. Olsen et al. 2011; Y. Fukui et al. 2017). Among these two possibilities, the colder and denser B3 might be “galactic fountain” flows, while B4 could originate from outside the LMC.

6. SUMMARY

In this paper, we present a detailed study of the properties of the CNM in and around the extreme star-forming region 30 Dor. To probe the CNM across 30 Dor, we made use of the high-resolution GASKAP-H I emission and absorption observations and spatially mapped various CNM properties (e.g., central velocities, optical depths, and average spin temperatures) on 7 pc scales. In addition, we compared the observed CNM properties to supplementary data to evaluate how the CNM changes in different environments and showed that the CNM is an important constituent of the baryon cycle in and around 30 Dor. Our key results are as follows.

1. H I absorption is clearly detected across $\sim 60 \text{ pc}$ scale regions, indicating the pervasiveness of the CNM in 30 Dor.
2. Four distinct CNM structures with systematically different characteristics exist at $200\text{--}230 \text{ km s}^{-1}$, $230\text{--}260 \text{ km s}^{-1}$, $260\text{--}277 \text{ km s}^{-1}$, and $277\text{--}300 \text{ km s}^{-1}$ (B1, B2, B3, and B4, respectively).

3. The CNM at B2 velocities belongs to the main dense structure of 30 Dor, where ionized, atomic, and molecular gases are concentrated. On the other hand, the CNM at B1 velocities traces outflows, while B3 and B4 are inflows with respect to 30 Dor. Compared to the CNM at B2 velocities, B1, B3, and B4 are warmer and have lower H I column densities.
4. Assuming simple spherically symmetric flows moving at a constant velocity, the outflow and inflow rates were estimated to be $0.007 M_{\odot} \text{ yr}^{-1}$ and $0.14 M_{\odot} \text{ yr}^{-1}$, respectively. The observed outflows and inflows are associated with a large amount of ionized gas, and hence the total outflow and inflow rates would be much higher than what we measured in H I. As for the origin of the gas flows, the outflows likely originate from active star formation in 30 Dor, while the inflows could be galactic fountain gas or be accreted from outside the LMC.
5. Compared to the high-latitude Milky Way and the less star-forming portion of the LMC, 30 Dor has systematically lower LOS average spin temperatures and higher H I column densities. The lower LOS average spin temperatures could result from a higher fraction of the CNM, which is expected in the extreme surroundings of 30 Dor where UV photons are abundant and thermal pressures are high.
6. The relatively uniform spatial distribution of the H I column densities at B1–B4 velocities indicates that H I shielding layers for H₂ formation exist in 30 Dor. Considering that the solar neighborhood and 30 Dor have significantly different ISM conditions, the presence of H I shielding layers in both environments suggests that dust grains play an important role in the H I-to-H₂ transition over a wide range of ISM conditions.

ACKNOWLEDGEMENTS

This scientific work uses data obtained from Inyarrimanha Ilgari Bundara/the Murchison Radio-astronomy Observatory. We acknowledge the Wajarri Yamaji People as the Traditional Owners and native title holders of the Observatory site. CSIRO’s ASKAP radio telescope is part of the Australia Telescope National Facility (<https://ror.org/05qajvd42>). Operation of ASKAP is funded by the Australian Government with support from the National Collaborative Research Infrastructure Strategy. ASKAP uses the resources of the Pawsey Supercomputing Research Centre. Establishment of ASKAP, Inyarrimanha Ilgari Bundara, the CSIRO Murchison Radio-astronomy Observatory and the Pawsey Supercomputing Research Centre are initiatives of the Australian

Government, with support from the Government of Western Australia, Australia and the Science and Industry Endowment Fund, Australia. GASKAP-H I is partially funded by the Australian Government through an Australian Research Council Australian Laureate Fellowship (project number FL210100039 awarded to NMc-G). The data to produce

the low-resolution H I emission were imaged using CHTC services at the University of Wisconsin’s Center for High Throughput Computing ([Center for High Throughput Computing 2006](http://data.csiro.au)). B.L. acknowledges support by the NRF, grant Nos. RS-2022-NR069020. This paper includes archived data obtained through the CSIRO ASKAP Science Data Archive, CASDA (<http://data.csiro.au>)

APPENDIX

A. THERMAL PRESSURES IN AND AROUND 30 DOR

Our H I observations along with the existing [C II] data provide us with a unique opportunity to measure the thermal pressure of the neutral ISM in and around 30 Dor. For our measurement of the thermal pressure, we followed the methodology of [P. F. Goldsmith et al. \(2018\)](#) and focused on B1, B3, and B4 where the contribution from ionized gas to [C II] emission is insignificant.

[P. F. Goldsmith et al. \(2018\)](#) analyzed the H I, [C II], and dust data toward four Galactic LOSs by assuming that [C II] emission is optically thin. In this case, the [C II] integrated intensity $W([C II])$ can be expressed as

$$W([C II]) \text{ (K km s}^{-1}\text{)} = 3.43 \times 10^{-16} N(C^+) \left[1 + 0.5 e^{91.21/T_k} \left(1 + \frac{2.4 \times 10^{-6}}{R_{ul} n} \right) \right]^{-1} \quad (A1)$$

where $N(C^+)$ is the C^+ column density, T_k is the gas kinetic temperature, R_{ul} is the de-excitation rate coefficient, n is the density of collisional partners, 91.21 K is the equivalent temperature, and $2.4 \times 10^{-6} \text{ s}^{-1}$ is the spontaneous decay rate of the [C II] line. In addition, all carbon was assumed to be singly ionized with a fixed fractional abundance so that the C^+ column density can be directly estimated from the total hydrogen column density.

When the [C II] excitation is done purely by collisions with atomic hydrogen, the following de-excitation rate coefficient can be adopted from [Ĝ. Barinova et al. \(2005\)](#) and [P. F. Goldsmith et al. \(2012\)](#):

$$R_{ul;H^0} = 7.6 \times 10^{-10} (T_k/100)^{0.14}. \quad (A2)$$

If the ratio of the C^+ column density to the integrated intensity is defined as $X = N(C^+)/W([C II])$, Equation A1 can be re-written as

$$n(H^0) \text{ (cm}^{-3}\text{)} = \frac{3.16 \times 10^3 (100/T_k)^{0.14}}{2e^{-91.21/T_k} (3.43 \times 10^{-16} X - 1) - 1}. \quad (A3)$$

The [C II] transition can also arise from the regions where both atomic and molecular hydrogens exist. In this case, the following effective de-excitation rate coefficient can be adopted

$$R_{ul;mix} = f_n(H^0)R_{ul;H^0} + f_n(H_2)R_{ul;H_2} \quad (A4)$$

where

$$R_{ul;H_2} = 10^{-10} [4.9 + 0.22(T_k/100)] \quad (A5)$$

and f_n is the fractional number densities of the two forms of hydrogen. With this effective de-excitation rate coefficient, Equation A1 can be re-written as

$$n(H^0 + H_2) \text{ (cm}^{-3}\text{)} = \frac{2.4 \times 10^{-6} R_{ul;mix}^{-1}}{2e^{-91.21/T_k} (3.43 \times 10^{-16} X - 1) - 1}. \quad (A6)$$

Before applying the methodology of [P. F. Goldsmith et al. \(2018\)](#) to 30 Dor, we examined if [C II] emission is indeed optically thin. According to [P. F. Goldsmith et al. \(2012\)](#), the medium is in the “effectively optically thin (EOT)” regime if the main-beam brightness temperature is lower than $\sim 1/3$ of the gas kinetic temperature (or $\lesssim 20\text{--}30$ K for typical interstellar clouds). In this case, the main-beam brightness temperature is linearly proportional to the C^+ column density regardless of the line opacity. The

measured peak main-beam brightness temperature of [C II] emission in 30 Dor reaches up to ~ 15 K only (Figure A1), suggesting that the [C II]-emitting gas is likely in the EOT regime.

Next, we estimated the molecular hydrogen column densities for B1, B3, and B4 based on the V -band dust extinction data from M. Y. Lee et al. (2019). To do so, we derived the total hydrogen column density for the foreground components (including B1, B2, B3, and B4; “Entire”) as follows:

$$\begin{aligned} N(\text{H})_{\text{f,Entire}} \text{ (cm}^{-2}\text{)} &= N(\text{H I})_{\text{f,Entire}} + 2N(\text{H}_2)_{\text{f,Entire}} \\ &= (5.56 \times 10^{21})qA_V \end{aligned} \quad (\text{A7})$$

Here we adopted the same $q = 0.5$ as we did for the determination of H I properties (Section 3.2) and the gas-to-dust ratio of $N(\text{H})/A_V = 5.56 \times 10^{21} \text{ cm}^{-2} \text{ mag}^{-1}$ for the LMC from J. L. Pineda et al. (2017). In addition, we scaled the $42''$ -scale A_V from M. Y. Lee et al. (2019) by $(30/42)^2$ to match the angular resolution of our H I data, assuming that dust grains uniformly fill the beams. To divide the total hydrogen column density into the individual velocity bands, we calculated the fractional contribution of each velocity band to the total atomic hydrogen column density $R_i = N(\text{H I})_{\text{f},i}/N(\text{H I})_{\text{f,Entire}}$ ($i = \text{B1, B3, and B4}$) and applied it to the total hydrogen column density as follows:

$$2N(\text{H}_2)_{\text{f},i} = R_i (N(\text{H})_{\text{f,Entire}} - N(\text{H I})_{\text{f,Entire}}). \quad (\text{A8})$$

We also derived the C^+ column densities for B1, B3, and B4 by applying the carbon fractional abundance of $[\text{C}/\text{H}] = 7.94 \times 10^{-5}$ for the LMC from R. J. Dufour et al. (1982) to the total hydrogen column density:

$$\begin{aligned} N(\text{C}^+)_{\text{f},i} &= 7.94 \times 10^{-5} N(\text{H})_{\text{f},i} \\ &= 7.94 \times 10^{-5} (N(\text{H I})_{\text{f},i} + 2N(\text{H}_2)_{\text{f},i}). \end{aligned} \quad (\text{A9})$$

With this C^+ column density, the ratio of the C^+ column density to the integrated intensity for B1, B3, and B4 can be estimated as follows:

$$\begin{aligned} X_{\text{f},i} &= \frac{N(\text{C}^+)_{\text{f},i}}{qW([\text{C II}])_i} \\ &= \frac{N(\text{C}^+)_{\text{f},i}}{0.5W([\text{C II}])_i}. \end{aligned} \quad (\text{A10})$$

To calculate the thermal pressure of the neutral ISM, we assumed that atomic and molecular hydrogens have the same number densities ($f_n(\text{H}^0) = f_n(\text{H}_2) = 0.5$) and kinetic temperatures ($T_k = \langle T_s \rangle$) and applied the corresponding Equations A4 and A10 to Equation A6. For our calculation, we selected the pixels where $N(\text{H I})_{\text{f},i}$, $N(\text{H})_{\text{f},i}$, and $W([\text{C II}])_{\text{f},i}$ ($i = \text{B1, B3, and B4}$) are higher than their 3σ uncertainties and present the results in Figures A2 and A3 and Table A1.

While keeping in mind the limitation of the simple assumptions in our calculation (e.g., $q = 0.5$, fixed gas-to-dust ratio, and same densities/temperatures for H^0 and H_2), we found that B1 has systematically higher thermal pressures than B3 and B4. For example, the median thermal pressure of $7.8 \times 10^4 \text{ cm}^{-3} \text{ K}$ for B1 is a factor of two higher than that of $(3.3\text{--}3.9) \times 10^4 \text{ cm}^{-3} \text{ K}$ for B3 and B4. The higher thermal pressures of B1 are consistent with the expectation for the observed weakness in H I emission (Section 5.2). Finally, we note that our estimates of $(0.7\text{--}36.7) \times 10^4 \text{ cm}^{-3} \text{ K}$ for B1, B3, and B4 are largely in agreement with J. L. Pineda et al. (2017), who found $(5.0\text{--}12.6) \times 10^4 \text{ cm}^{-3} \text{ K}$ for the LOSs associated with 30 Dor based on the same methodology as ours except for few differences (e.g., different densities/temperatures for H^0 and H_2).

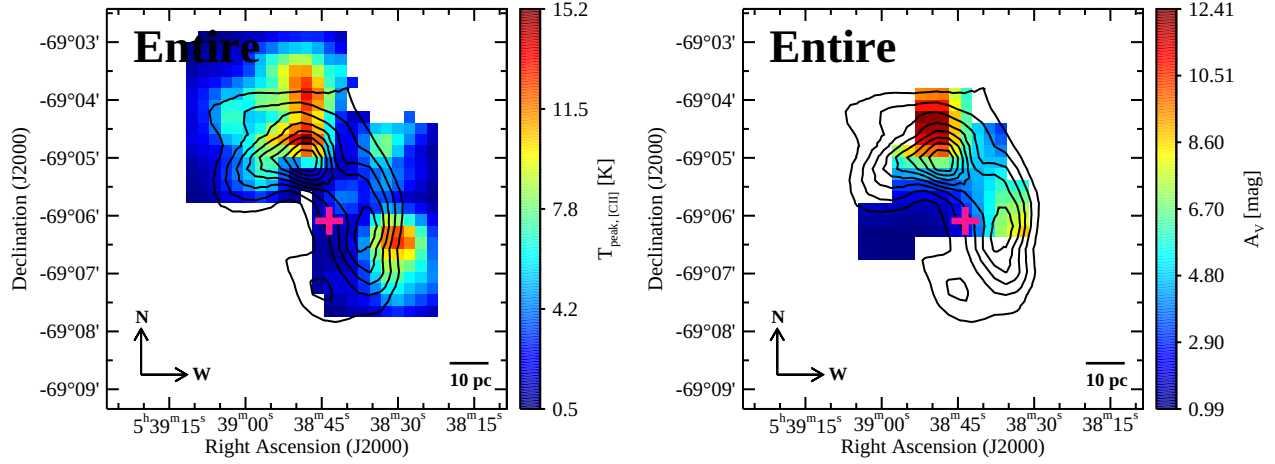


Figure A1. Spatial distributions of the [C II] peak brightness temperature (left; 30'' scales) and V-band dust extinction (right; 42'' scales). The entire velocity range was considered for the [C II] peak temperature, while the dust extinction was scaled by $(30/42)^2$ to match the angular resolution of the H I data. For both images, 1.4 GHz continuum emission is overlaid as the contours with levels ranging from 20% to 90% of the peak value (448 K) in steps of 10%, and the location of R136 is indicated as the red cross.

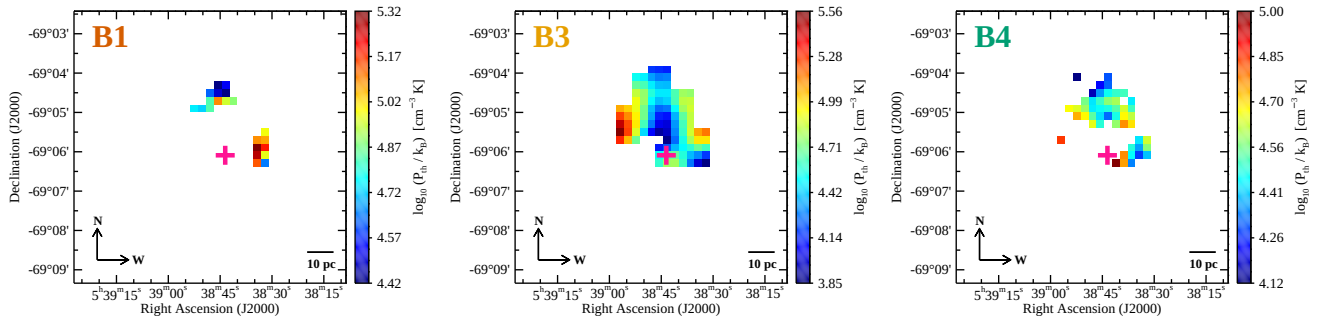


Figure A2. Spatial distribution of the thermal pressure for each velocity band (B1, B3, and B4). All three maps have an angular resolution of 30'' with a pixel size of 12'', and the location of R136 is indicated as the red cross.

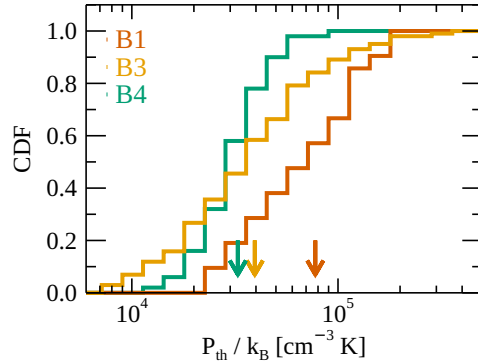


Figure A3. CDFs of the thermal pressures. The median of each distribution is marked as the arrow.

Table A1. Results for B1, B3, and B4

| Band | # of Pixels | $\langle T_s \rangle$ (K) | $2N(\text{H}_2)_f$ (10^{21} cm^{-2}) | $f(\text{H}_2)_f$ | $qW(\text{C II})$ (K km s $^{-1}$) | X_f ($10^{16} \text{ cm}^{-2} (\text{K km s}^{-1})^{-1}$) | P_{th}/k_B ($10^4 \text{ cm}^{-3} \text{ K}$) |
|------|-------------|------------------------------|-----------------------------------------------------|-------------------|----------------------------------------|------------------------------------------------------------------|-------------------------------------------------------------|
| (1) | (2) | (3) | (4) | (5) | (6) | (7) | (8) |
| B1 | 21 | 43.6–138.4 80.6 | 0.5–1.3 0.9 | 0.79–0.91 0.84 | 1.7–5.1 2.8 | 1.4–5.9 3.1 | 2.6–20.7 7.8 |
| B3 | 101 | 72.0–183.1 114.9 | 0.9–10.9 4.3 | 0.47–0.91 0.81 | 1.3–31.1 8.5 | 1.2–22.9 4.5 | 0.7–36.7 3.9 |
| B4 | 50 | 200.5–558.7 310.7 | 0.5–4.3 2.1 | 0.53–0.91 0.83 | 1.4–5.2 2.7 | 2.4–20.4 7.8 | 1.3–9.9 3.3 |

NOTE—(1) Velocity band; (2) Number of pixels that were considered for the derivation of the thermal pressure. These pixels were selected to have $N(\text{H I})_f$, $N(\text{H})_f$, and $W(\text{C II})_f > 3\sigma$ uncertainties. For B1, two pixels with negative thermal pressures were masked; (3) LOS average spin temperature; (4) Dust-based H_2 column density (Equation A8). The derived H_2 column densities are all higher than 3σ uncertainties; (5) Molecular fraction, as defined by $2N(\text{H}_2)/N(\text{H})_f$; (6) $[\text{C II}]$ integrated intensity; (7) Ratio of the C^+ column density to the integrated intensity (Equation A10); (8) Thermal pressure. For each of the columns (3)–(8), the range and median value for the selected pixels are listed.

REFERENCES

- Barinovs, Ģ., van Hemert, M. C., Krems, R., & Dalgarno, A. 2005, *ApJ*, 620, 537, doi: [10.1086/426860](https://doi.org/10.1086/426860)
- Bialy, S. 2020, *ApJ*, 903, 62, doi: [10.3847/1538-4357/abb804](https://doi.org/10.3847/1538-4357/abb804)
- Bialy, S., & Sternberg, A. 2016, *ApJ*, 822, 83, doi: [10.3847/0004-637X/822/2/83](https://doi.org/10.3847/0004-637X/822/2/83)
- Bialy, S., & Sternberg, A. 2019, *ApJ*, 881, 160, doi: [10.3847/1538-4357/ab2fd1](https://doi.org/10.3847/1538-4357/ab2fd1)
- Bialy, S., Sternberg, A., Lee, M.-Y., Le Petit, F., & Roueff, E. 2015, *ApJ*, 809, 122, doi: [10.1088/0004-637X/809/2/122](https://doi.org/10.1088/0004-637X/809/2/122)
- Bühr, S., Beuther, H., Ott, J., et al. 2015, *A&A*, 580, A112, doi: [10.1051/0004-6361/201425370](https://doi.org/10.1051/0004-6361/201425370)
- CASA Team, Bean, B., Bhatnagar, S., et al. 2022, *PASP*, 134, 114501, doi: [10.1088/1538-3873/ac9642](https://doi.org/10.1088/1538-3873/ac9642)
- Center for High Throughput Computing. 2006, Center for High Throughput Computing, doi: [10.21231/GNT1-HW21](https://doi.org/10.21231/GNT1-HW21)
- Chevance, M., Madden, S. C., Lebouteiller, V., et al. 2016, *A&A*, 590, A36, doi: [10.1051/0004-6361/201527735](https://doi.org/10.1051/0004-6361/201527735)
- Chevance, M., Kruijssen, J. M. D., Hygate, A. P. S., et al. 2020, *MNRAS*, 493, 2872, doi: [10.1093/mnras/stz3525](https://doi.org/10.1093/mnras/stz3525)
- Chu, Y.-H., & Kennicutt, Jr., R. C. 1994, *ApJ*, 425, 720, doi: [10.1086/174017](https://doi.org/10.1086/174017)
- Cornwell, T. J. 2008, *IEEE Journal of Selected Topics in Signal Processing*, 2, 793, doi: [10.1109/JSTSP.2008.2006388](https://doi.org/10.1109/JSTSP.2008.2006388)
- Crowther, P. A., Schnurr, O., Hirschi, R., et al. 2010, *MNRAS*, 408, 731, doi: [10.1111/j.1365-2966.2010.17167.x](https://doi.org/10.1111/j.1365-2966.2010.17167.x)
- Dickey, J. M., Mebold, U., Stanimirovic, S., & Staveley-Smith, L. 2000, *ApJ*, 536, 756, doi: [10.1086/308953](https://doi.org/10.1086/308953)
- Dickey, J. M., McClure-Griffiths, N., Gibson, S. J., et al. 2013, *PASA*, 30, e003, doi: [10.1017/pasa.2012.003](https://doi.org/10.1017/pasa.2012.003)
- Doran, E. I., Crowther, P. A., de Koter, A., et al. 2013, *A&A*, 558, A134, doi: [10.1051/0004-6361/201321824](https://doi.org/10.1051/0004-6361/201321824)
- Draine, B. T. 1978, *ApJS*, 36, 595, doi: [10.1086/190513](https://doi.org/10.1086/190513)
- Dufour, R. J., Shields, G. A., & Talbot, Jr., R. J. 1982, *ApJ*, 252, 461, doi: [10.1086/159574](https://doi.org/10.1086/159574)
- Fukui, Y., Tsuge, K., Sano, H., et al. 2017, *PASJ*, 69, L5, doi: [10.1093/pasj/psx032](https://doi.org/10.1093/pasj/psx032)
- Goldsmith, P. F., Langer, W. D., Pineda, J. L., & Velusamy, T. 2012, *ApJS*, 203, 13, doi: [10.1088/0067-0049/203/1/13](https://doi.org/10.1088/0067-0049/203/1/13)
- Goldsmith, P. F., Pineda, J. L., Neufeld, D. A., et al. 2018, *ApJ*, 856, 96, doi: [10.3847/1538-4357/aab34e](https://doi.org/10.3847/1538-4357/aab34e)
- Guzman, J., Whiting, M., Voronkov, M., et al. 2019, *ASKAPsoft: ASKAP science data processor software*, Astrophysics Source Code Library, record ascl:1912.003 <http://ascl.net/1912.003>
- Hall, K. P., Stanimirović, S., Lee, M.-Y., Wolfire, M., & Goldsmith, P. 2020, *ApJ*, 899, 23, doi: [10.3847/1538-4357/ab9b86](https://doi.org/10.3847/1538-4357/ab9b86)
- Haynes, R. F., Klein, U., Wielebinski, R., & Murray, J. D. 1986, *A&A*, 159, 22
- Heiles, C., & Troland, T. H. 2003, *ApJ*, 586, 1067, doi: [10.1086/367828](https://doi.org/10.1086/367828)
- Hotan, A. W., Bunton, J. D., Chippendale, A. P., et al. 2021, *PASA*, 38, e009, doi: [10.1017/pasa.2021.1](https://doi.org/10.1017/pasa.2021.1)
- Indebetouw, R., Brogan, C., Chen, C. H. R., et al. 2013, *ApJ*, 774, 73, doi: [10.1088/0004-637X/774/1/73](https://doi.org/10.1088/0004-637X/774/1/73)
- Jenkins, E. B., & Tripp, T. M. 2011, *ApJ*, 734, 65, doi: [10.1088/0004-637X/734/1/65](https://doi.org/10.1088/0004-637X/734/1/65)
- Kalberla, P. M. W., & Haud, U. 2015, *A&A*, 578, A78, doi: [10.1051/0004-6361/201525859](https://doi.org/10.1051/0004-6361/201525859)
- Kennicutt, R. C., & Evans, N. J. 2012, *ARA&A*, 50, 531, doi: [10.1146/annurev-astro-081811-125610](https://doi.org/10.1146/annurev-astro-081811-125610)
- Kim, J., Chevance, M., Kruijssen, J. M. D., et al. 2022, *MNRAS*, 516, 3006, doi: [10.1093/mnras/stac2339](https://doi.org/10.1093/mnras/stac2339)
- Kim, S., Dopita, M. A., Staveley-Smith, L., & Bessell, M. S. 1999, *AJ*, 118, 2797, doi: [10.1086/301116](https://doi.org/10.1086/301116)
- Kruijssen, J. M. D., & Longmore, S. N. 2014, *MNRAS*, 439, 3239, doi: [10.1093/mnras/stu098](https://doi.org/10.1093/mnras/stu098)
- Krumholz, M. R., & McKee, C. F. 2005, *ApJ*, 630, 250, doi: [10.1086/431734](https://doi.org/10.1086/431734)
- Lee, M.-Y., Stanimirović, S., Murray, C. E., Heiles, C., & Miller, J. 2015, *ApJ*, 809, 56, doi: [10.1088/0004-637X/809/1/56](https://doi.org/10.1088/0004-637X/809/1/56)
- Lee, M.-Y., Stanimirović, S., Douglas, K. A., et al. 2012, *ApJ*, 748, 75, doi: [10.1088/0004-637X/748/2/75](https://doi.org/10.1088/0004-637X/748/2/75)
- Lee, M. Y., Madden, S. C., Le Petit, F., et al. 2019, *A&A*, 628, A113, doi: [10.1051/0004-6361/201935215](https://doi.org/10.1051/0004-6361/201935215)
- McClure-Griffiths, N. M., Pisano, D. J., Calabretta, M. R., et al. 2009, *ApJS*, 181, 398, doi: [10.1088/0067-0049/181/2/398](https://doi.org/10.1088/0067-0049/181/2/398)
- McClure-Griffiths, N. M., Dénes, H., Dickey, J. M., et al. 2018, *Nature Astronomy*, 2, 901, doi: [10.1038/s41550-018-0608-8](https://doi.org/10.1038/s41550-018-0608-8)
- McKee, C. F., & Ostriker, J. P. 1977, *ApJ*, 218, 148, doi: [10.1086/155667](https://doi.org/10.1086/155667)
- Meixner, M., Gordon, K. D., Indebetouw, R., et al. 2006, *AJ*, 132, 2268, doi: [10.1086/508185](https://doi.org/10.1086/508185)
- Murray, C. E., Stanimirović, S., Goss, W. M., et al. 2018, *ApJS*, 238, 14, doi: [10.3847/1538-4365/aad81a](https://doi.org/10.3847/1538-4365/aad81a)
- Nayak, O., Green, A., Hirschauer, A. S., et al. 2023, *ApJ*, 944, 26, doi: [10.3847/1538-4357/acac8b](https://doi.org/10.3847/1538-4357/acac8b)
- Nguyen, H., Dawson, J. R., Lee, M.-Y., et al. 2019, *ApJ*, 880, 141, doi: [10.3847/1538-4357/ab2b9f](https://doi.org/10.3847/1538-4357/ab2b9f)
- Offringa, A. R., McKinley, B., Hurley-Walker, N., et al. 2014, *MNRAS*, 444, 606, doi: [10.1093/mnras/stu1368](https://doi.org/10.1093/mnras/stu1368)
- Okada, Y., Güsten, R., Requena-Torres, M. A., et al. 2019, *A&A*, 621, A62, doi: [10.1051/0004-6361/201833398](https://doi.org/10.1051/0004-6361/201833398)
- Olsen, K. A. G., Zaritsky, D., Blum, R. D., Boyer, M. L., & Gordon, K. D. 2011, *ApJ*, 737, 29, doi: [10.1088/0004-637X/737/1/29](https://doi.org/10.1088/0004-637X/737/1/29)
- Park, G., Lee, M.-Y., Bialy, S., et al. 2023, *ApJ*, 955, 145, doi: [10.3847/1538-4357/ace164](https://doi.org/10.3847/1538-4357/ace164)
- Pellegrini, E. W., Baldwin, J. A., & Ferland, G. J. 2010, *ApJS*, 191, 160, doi: [10.1088/0067-0049/191/1/160](https://doi.org/10.1088/0067-0049/191/1/160)

- Pietrzyński, G., Graczyk, D., Gieren, W., et al. 2013, *Nature*, 495, 76, doi: [10.1038/nature11878](https://doi.org/10.1038/nature11878)
- Pineda, J. L., Langer, W. D., Goldsmith, P. F., et al. 2017, *ApJ*, 839, 107, doi: [10.3847/1538-4357/aa683a](https://doi.org/10.3847/1538-4357/aa683a)
- Pingel, N. M., Dempsey, J., McClure-Griffiths, N. M., et al. 2022, *PASA*, 39, e005, doi: [10.1017/pasa.2021.59](https://doi.org/10.1017/pasa.2021.59)
- Poudel, S., Horton, A., Vazquez, J., et al. 2025, arXiv e-prints, arXiv:2503.05968, doi: [10.48550/arXiv.2503.05968](https://doi.org/10.48550/arXiv.2503.05968)
- Roman-Duval, J., Gordon, K. D., Meixner, M., et al. 2014, *ApJ*, 797, 86, doi: [10.1088/0004-637X/797/2/86](https://doi.org/10.1088/0004-637X/797/2/86)
- Russell, S. C., & Dopita, M. A. 1992, *ApJ*, 384, 508, doi: [10.1086/170893](https://doi.org/10.1086/170893)
- Rybarczyk, D. R., Stanimirović, S., Gong, M., et al. 2022, *ApJ*, 928, 79, doi: [10.3847/1538-4357/ac5035](https://doi.org/10.3847/1538-4357/ac5035)
- Selman, F. J., & Melnick, J. 2013, *A&A*, 552, A94, doi: [10.1051/0004-6361/201220396](https://doi.org/10.1051/0004-6361/201220396)
- Stanimirović, S., Murray, C. E., Lee, M.-Y., Heiles, C., & Miller, J. 2014, *ApJ*, 793, 132, doi: [10.1088/0004-637X/793/2/132](https://doi.org/10.1088/0004-637X/793/2/132)
- Sternberg, A., Le Petit, F., Roueff, E., & Le Bourlot, J. 2014, *ApJ*, 790, 10, doi: [10.1088/0004-637X/790/1/10](https://doi.org/10.1088/0004-637X/790/1/10)
- Townsley, L. K., Broos, P. S., Feigelson, E. D., et al. 2006, *AJ*, 131, 2140, doi: [10.1086/500532](https://doi.org/10.1086/500532)
- van der Tol, S., Veenboer, B., & Offringa, A. R. 2018, *A&A*, 616, A27, doi: [10.1051/0004-6361/201832858](https://doi.org/10.1051/0004-6361/201832858)
- Wolfire, M. G., McKee, C. F., Hollenbach, D., & Tielens, A. G. G. M. 2003, *ApJ*, 587, 278, doi: [10.1086/368016](https://doi.org/10.1086/368016)
- Wong, T., Oudshoorn, L., Sofovich, E., et al. 2022, *ApJ*, 932, 47, doi: [10.3847/1538-4357/ac723a](https://doi.org/10.3847/1538-4357/ac723a)